

# The Cetus-Palca stream: A disrupted small dwarf galaxy

## A prequel to the science possible with WEAVE with precise spectro-photometric distances

Guillaume F. Thomas<sup>1,2</sup>, Giuseppina Battaglia<sup>1,2</sup>

<sup>1</sup> Instituto de Astrofísica de Canarias, E-38205 La Laguna, Tenerife, Spain

<sup>2</sup> Universidad de La Laguna, Dpto. Astrofísica, E-38206 La Laguna, Tenerife, Spain  
e-mail: gthomas@iac.es

Accepted on December 1, 2021

### ABSTRACT

We present a new fully data-driven approach to derive spectro-photometric distances based on artificial neural networks. The method was developed and tested on SEGUE data and will serve as a reference for the *Contributed Data Product* SPDIST of the WEAVE survey. With this method, the relative precision of the distances is of  $\sim 13\%$ . The catalogue of more than 300,000 SEGUE stars for which we have derived spectro-photometric distances will soon be publicly available on the *Vizier* service of the Centre de Données de Strasbourg. With this 6D catalogue of stars with positions, distances, line-of-sight velocity, and *Gaia* proper motions, we were able to identify stars belonging to the Cetus stellar stream in the integrals of motion space. Guided by the properties we derived for the Cetus stream from this 6D sample, we searched for additional stars from the blue horizontal and from the red giant branches in a 5D sample. We find that the Cetus stream and the Palca overdensity are actually two parts of the same structure, which therefore we propose to rename the Cetus-Palca stream. We found that the Cetus-Palca stream has a stellar mass of  $\approx 1.5 \times 10^6 M_{\odot}$  and presents a prominent distance gradient of 15 kpc over the  $\sim 100^{\circ}$  that it covers on the sky. Additionally, we also report the discovery of a second structure, almost parallel to the Cetus stream, covering  $\sim 50^{\circ}$  of the sky, that could potentially be a stellar stream formed by the tidal disruption of a globular cluster that was orbiting around the Cetus stream progenitor.

**Key words.** Galaxy: halo – Galaxy: kinematics and dynamics – stars: distances – methods: data analysis – catalogs

### 1. Introduction

Large astrometric and spectroscopic surveys, such as *Gaia* (Gaia Collaboration 2016; Gaia Collaboration 2018), WEAVE (Dalton et al. 2012), DESI (Flaugher & Bebek 2014), SDSS (Kollmeier et al. 2017), LAMOST (Zhao et al. 2012) or H3 (Conroy et al. 2019a), are providing chemical and kinematic properties for a tremendous number of individual stars in our Galaxy. With these data, it is possible to reconstruct in detail the formation history of the Milky Way (e.g. Belokurov et al. 2018; Haywood et al. 2018; Kruijssen et al. 2020; Naidu et al. 2020; Fernández-Alvar et al. 2021; Ishigaki et al. 2021; Lane et al. 2021; Malhan et al. 2021; Simpson et al. 2021) and to compare it to the formation histories of similar galaxies in large scale cosmological simulations. Precise distances of individual stars are a crucial ingredient in the determination of the structure and kinematic properties of the Milky Way stellar component, e.g. to transform *Gaia* proper motions into physical tangential velocities. However, despite the great advances brought about by the European Space Agency's *Gaia* mission to provide parallaxes for more than 1.4 billions stars (Gaia Collaboration 2016; Gaia Collaboration et al. 2020), these do not have the sufficient precision to measure the distance of stars beyond  $\sim 10$  kpc (e.g. Ibata et al. 2017), i.e. located in the outer disc or in most of the stellar halo; therefore, other methods are needed, to enable an investigation of the properties of the outskirts of the Milky Way.

Several methods have been developed to infer distances, either using only photometric data (e.g. Jurić et al. 2008; Ivezić

et al. 2008; Deason et al. 2011; Ibata et al. 2017; Sesar et al. 2017; Thomas et al. 2019b; Conroy et al. 2021) or a combination of spectroscopic and photometric data (e.g. Xue et al. 2014; Coronado et al. 2018; McMillan et al. 2018; Queiroz et al. 2018; Hogg et al. 2018; Cargile et al. 2020). Some developed methods infer statistically the distances of the stars, based on the assumptions made on the global distribution of the stars in the Galaxy (e.g. Bailer-Jones 2015; Bailer-Jones et al. 2018; Queiroz et al. 2018; Anders et al. 2019; Pierses et al. 2019). However, these methods depend sensitively on the adopted Galactic spatial distribution prior (Hogg et al. 2018), which is still not precisely known, especially in the stellar halo, as different tracers yield different trends (Thomas et al. 2018; Fukushima et al. 2019). The methods to obtain photometric distances do not require (expensive) spectroscopic measurements, at the price of being often limited to specific stellar populations. These are not always easy to identify photometrically, leading to potentially strong biases. Spectrophotometric methods tend to be more accurate since they use both photometric and spectroscopic information. However, most of them are still focused on specific stellar populations (K-giants: Xue et al. 2014, main sequence stars: Coronado et al. 2018, red giant branch stars: Hogg et al. 2018), and the majority of them are based on theoretical spectro-photometric relations (e.g. Xue et al. 2014; McMillan et al. 2018; Queiroz et al. 2018; Cargile et al. 2020).

Thanks to the *Gaia* early third data release (EDR3 Gaia Collaboration et al. 2020), it is now possible to develop new methods to derive spectro-photometric distances by using the

large number of stars with spectroscopic data and precise parallaxes; this can be potentially done for stars from different stellar evolutionary phases and without relying on theoretical spectro-photometric models. We present here a new data-driven method to measure precisely distances using spectroscopic and photometric information using Machine Learning (ML) techniques. This method is heavily based on the previous work described in [Thomas et al. \(2019b\)](#); the major difference is the use here of spectroscopic parameters (gravity, effective temperature and metallicity), which improve the distance measurements, especially for giant stars, and the absence of the  $u$ -band photometry from the Canada-France-Imaging-Survey (CFIS/UNIONS [Ibata et al. 2017](#)). Our primary objective was to develop the method and the algorithm that will be used to provide spectro-photometric distances for the stars observed by WEAVE as the WEAVE Contributed Data Product<sup>1</sup> (CDP) SP<sub>DIST</sub>. However, at the time of writing, WEAVE is not yet operational. Therefore, we developed our method using stars observed by the Sloan Extension for Galactic Understanding and Exploration survey (SEGUE [Yanny et al. 2009](#)), since, among the publicly available spectroscopic datasets, it is the closest one to what WEAVE will deliver, in terms of instrumental specifications in its low-resolution mode. The dataset, the architecture of the algorithm and the validation of the precision on the distance achieved with this method are presented in Section 2. We applied this algorithm to derive spectro-photometric distances for more than 300,000 stars present in SEGUE, whose catalogue will soon be publicly available here. In Sect. 3 we present the identification of the Cetus stream as a structure in the integral-of-motion space using 6D information for SEGUE stars, including the spectro-photometric distances derived in this work. In Section 4 we used the information gained by integrating the orbit of the stars of the Cetus stream as a guide to expand the search to the more numerous sample of stars with 5D information: first we focus on blue horizontal branch stars (in Section 4.2.2), and then with the different stellar populations of Cetus present in *Gaia* EDR3. Finally, we present our conclusions in Section 5.

## 2. Determination of spectro-photometric distances

In this section, we present a new ML-based method to determine the distance of individual stars through their spectro-photometric parameters. Contrary to [Cargile et al. \(2020\)](#), who used mock data to fit their spectro-photometric distance relation, this method uses a data-driven approach.

### 2.1. Data

We train and apply the method to the stars observed by the SEGUE survey ([Yanny et al. 2009](#)). From the SEGUE stellar catalogue, only stars with a photometric counterpart in the second data release of the Pan-STARRS1  $3\pi$  Steradian survey (PS1 [Chambers et al. 2016](#)) and in *Gaia* EDR3 are used hereafter. More specifically, we used the forced-WARP PSF photometry in the *griz*-bands from PS1 ([Magnier et al. 2020a](#)) and the  $G$ -band from EDR3. The PS1  $y$ -band is not used due to its shallowness compared to the other bands, and the *Gaia*  $G_{BP}$  and  $G_{RP}$  due to the excess of colour at the faintest magnitudes, correlated with large uncertainties. Although, this is not very important for SEGUE stars, because this survey has a depth of  $G \sim 18$ , it is important to already take this point into account since WEAVE is

<sup>1</sup> A *Contributed Data Product* is a product beyond what the WEAVE Advanced Processing System will provide.

expected to go down to the *Gaia* magnitude limit in the Galactic archaeology sub-survey of the thick disc and stellar halo at low spectral resolution, as presented in the [WEAVE science case](#).

All the stars are corrected from the foreground extinction assuming the  $E(B - V)$  values given by [Schlegel et al. \(1998\)](#) at the star's position, with the reddening conversion coefficients for the *griz*-bands given by [Schlafly & Finkbeiner \(2011\)](#) for a reddening parameter of  $R_v = 3.1$ , while for the *Gaia*  $G$  filter, we follow [Sestito et al. \(2019\)](#) by adopting the coefficients from [Marigo et al. \(2008\)](#). It has to be noticed that some stars from this cross-matched catalogue are affected by crowding in dense regions (i.e. globular clusters) especially with the PS1 forced-WARP photometry used here. Therefore, to prevent any biases generated by those stars as well as to remove extended objects such as background galaxies, we keep only the stars with  $|STARGAL| < 3$ . The STARGAL parameter is the median (in sigma) of the difference between the Kron and the PSF photometry compared to their uncertainties added in quadrature for all single-exposures of a single object (see [Magnier et al. 2020a,b](#)).

### 2.2. The method

Our algorithm uses the spectroscopically determined effective temperature ( $T_{eff}$ ), surface gravity ( $\log(g)$ ) and metallicity ( $[Fe/H]$ ) with a combination of photometric colours to estimate the absolute magnitude in the *Gaia*  $G$ -band for each star, and therefore its distance, through an Artificial Neural Network (ANN). To perform this so-called regression, the inputs of the ANN are the TEFFADOP, LOGGADOP and FEHANNRR parameters from the SEGUE Stellar Parameters Pipeline (SSPP [Lee et al. 2008](#)), and all the possible colours that can be produced from the  $g_0, r_0, i_0, z_0$  and  $G_0$  extinction corrected photometry<sup>2</sup>. We choose not to use the FEHADOP metallicity since it is a combination of metallicity derived by different methods, which tend to erase the signal in the tails of the distribution (see their Appendix A of [Starkenburger et al. 2017](#)). Following [Starkenburger et al. \(2017\)](#), we decided to use the FEHANNRR parameter because it provides a more robust estimate, particularly at the low metallicity regime, where are the bulk of the halo stars. In order to improve the performance of the ANN and to limit the potential biases, all the input parameters are normalized to have a distribution with a mean equal to zero and a standard deviation of one with respect to the training sample.

To train and test an ANN, it is advantageous to use a training set as large as possible. However, the training set has to be composed of stars with precise parameters, to prevent a false relation to be learnt by the algorithm due to objects with imprecise parameters. Therefore, we imposed a signal-to-noise ratio cut of  $SNR \geq 20$  for the stars in the training sample. This threshold was chosen because at lower SNR, the distribution of the uncertainties on the parameters given by the SSPP as a function of the SNR is irregular, indicating that the parameters in that region are not reliable (see discussion in [Thomas et al. 2019b](#)).

Because the surface gravity plays a key role in disentangling main-sequence and red giant branch (RGB) stars, which at the same colour have very different absolute magnitudes, we only consider stars with uncertainties  $\delta \log(g) < 0.2$  dex for the training sample, i.e. approximately below the typical internal uncertainty on LOGGADOP (0.19 dex according to [Lee et al. 2008](#)).

Furthermore, we kept only stars with photometric uncertainties in all the bands better than 0.1 mag.

<sup>2</sup> i.e.  $(g-r)_0, (g-i)_0, (g-z)_0, (r-i)_0, (r-z)_0, (i-z)_0, (g-G)_0, (G-r)_0, (G-i)_0$  and  $(G-z)_0$

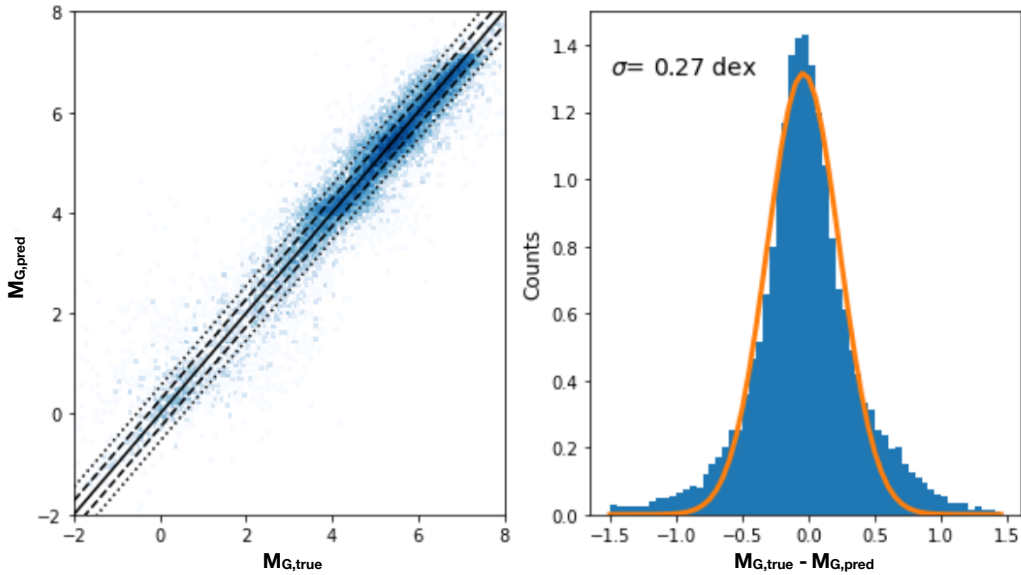


**Fig. 1.** Comparison of the “true” ( $M_{G,true}$ ) and predicted ( $M_{G,pred}$ ) absolute magnitude for the stars of the training sample. The left panel shows the true and derived quantities plotted against each other. The one-to-one relation is shown as a solid line, and the dashed and dotted lines correspond respectively to the  $1 - \sigma$  and  $2 - \sigma$  deviation. The right panel shows the distribution of the difference between the true and derived absolute magnitude, with a Gaussian fit overlaid. A scatter of 0.27 magnitude corresponds to a relative uncertainty on the distance of 13%.

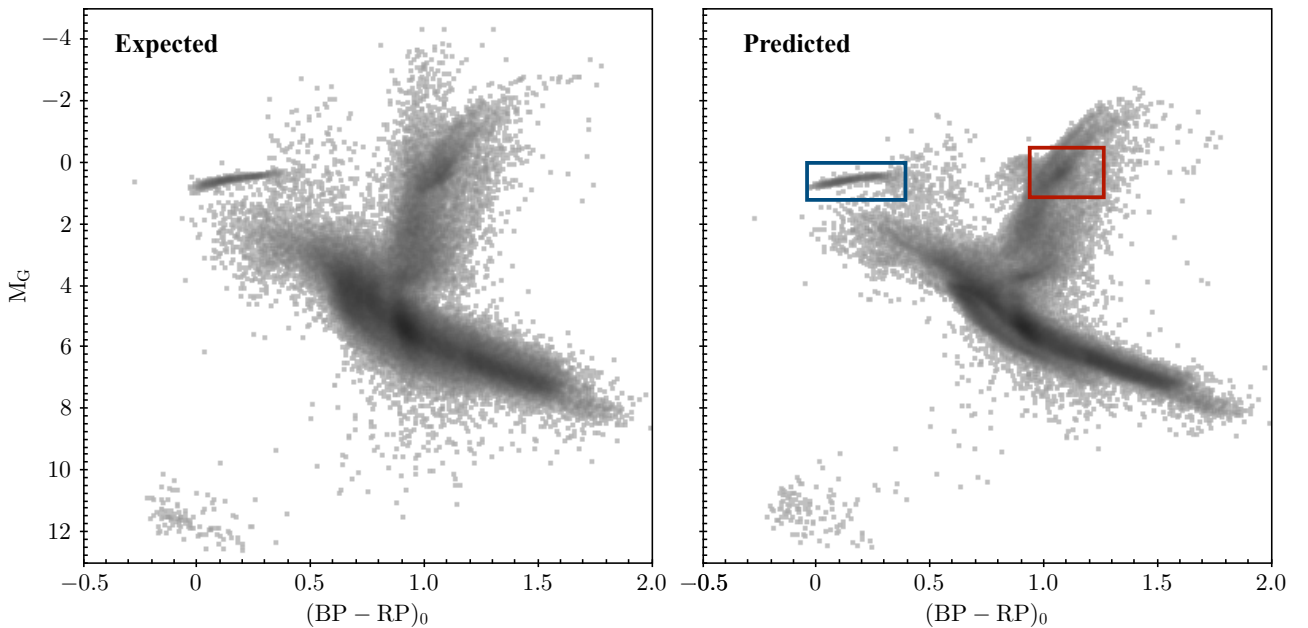


**Fig. 2.** Colour-Magnitude diagram (CMD) of the training sample with the expected absolute magnitude in the *Gaia*  $G$ -band shown on the left panel, and with the absolute magnitude predicted by the algorithm on the right panel. It is striking to see clearly the red clump (RC) on the predicted CMD highlighted by the red box, while this feature it is less obvious on the expected CMD. We also highlighted with the blue rectangle the location of the blue horizontal branch (BHB) stars, which were added in the training sample as explained in Section 2.2.

The absolute magnitudes on which the ANN is trained are obtained from *Gaia* parallaxes ( $\varpi$ ), such as  $M_G = G_0 + 5 + 5 \log_{10}(\varpi [\text{mas}]/1000)$ . We correct *Gaia* parallaxes from the zero point off-set as a function of colour and sky location, following Lindegren et al. (2020). This method imposes a positive zero-point corrected parallax on the stars of the training sample. Thus, we only keep stars with a minimum parallax of  $\varpi = 0.1$

$\text{mas yr}^{-1}$ , as stars with a smaller parallax tend to have unrealistic absolute magnitude (Luri et al. 2018; Thomas et al. 2019a).

As show by Luri et al. (2018), the inversion of the parallax to obtain the distance (and so the absolute magnitude), is only valid for relative parallax uncertainties  $\varpi/\delta\varpi \geq 5$  (or a relative distance precision better than 20%). For the dwarf stars ( $\log(g) \geq 3.5$ ), which are largely from the main-sequence (MS), this is not a problem since 104,516 dwarf stars respect this cri-



terion, covering a wide range of metallicity and temperature. However, as mentioned by [Thomas et al. \(2019a\)](#), using this relative parallax precision criteria also on giant stars ( $\log(g) < 3.5$ ) would limit the sample to only  $\sim 3,000$  stars. Furthermore, these are even not representative of the full giant sample of the SEGUE dataset, as most are sub-giant stars, with  $\log(g) \sim 3$ . The reason for this difference between dwarf and giant stars is that at a similar apparent magnitude, the giants are more distant than the dwarfs, which leads to a higher uncertainty in their parallax. Thus, following [Hogg et al. \(2018\)](#) and [Thomas et al. \(2019a\)](#), instead of imposing a relative precision cut on the parallax for giants stars, we keep only those with  $\delta\varpi < 0.07$  mas.

We also used 4,625 of the 6036 K-giants from the catalogue of [Xue et al. \(2014\)](#) (the other 1,400 do not respect the photometric uncertainties criteria in all the bands), which have distance measurements with a relative precision of 16%. This additional dataset marks a great improvement compared to [Thomas et al. \(2019a\)](#), especially for the intrinsically brightest stars in SEGUE, by adding a large number of giant stars with precise distances. For the K-giants from the [Xue et al. \(2014\)](#) catalogue that pass the  $\delta\varpi < 0.07$  mas cut, we used the (Maximum Likelihood) distance modulus (DM) provided by [Xue et al. \(2014\)](#) rather than using the *Gaia* parallax to infer the absolute magnitude used to train the ANN. A total of 14,826 giant stars compose the training set, of which 10,201 have been selected based on their *Gaia* parallax.

The blue horizontal branch (BHB) stars present in the training sample, which can be identified through their location on the colour magnitude diagram (CMD) on Fig. 2, have large uncertainties on their parallax, leading to a broad range of "true" absolute magnitudes. We find that our algorithm is actually able to recover a BHB, likely thanks to the input spectroscopic surface gravity. However, the intrinsic brightness tends to be underestimated, such that the distance of these BHBs is overestimated by a factor  $\sim 1.1$  when compared to the distances obtained from the relation of [Deason et al. \(2011\)](#), based on SDSS photometry in the  $g$  and  $r$ -bands. Therefore, we decided to add BHB stars from the catalogue of [Xue et al. \(2008\)](#) to the training sample, with the absolute magnitude derived using the relation of [Deason et al. \(2011\)](#). This finally leads to a training sample composed of 14,826 giant stars, of 104,321 dwarf stars and of 1,376 BHB stars. The impact of adding the K-giants of [Xue et al. \(2014\)](#) and the BHBs of [Xue et al. \(2008\)](#) to the training sample on the precisions of the predicted distances is discussed in Appendix A.

By itself, the architecture of the ANN is rather classical. It is composed of 4 hidden layers composed of respectively 2048, 512, 64 and 32 neurons using a Rectified Linear Unit (ReLU) activation function, build with the KERAS package ([Chollet 2015](#)). Due to the large number of possible outliers (especially for giant stars), the cost function used by the ANN is a Mean Squared-Error (MSE), coupled to an Adaptive Moment Estimation (also known as Adam) optimization method ([Kingma & Ba 2014](#)) to prevent falling to a local minimum.

The difference between the predicted and the "true" absolute magnitude (used to train the ANN) is shown in Figure 1. The residual is of  $\sigma = 0.27$  mag, corresponding to a relative distance precision of 13%, and does not show any trend with the absolute magnitude. Notwithstanding the inhomogeneities of the training sample, it seems reasonable to think that the 13% precision is an upper limit when comparing the CMD built from the "true" absolute magnitude (Fig. 2, left) and that made from the predicted absolute magnitude (Fig. 2, right). Indeed, not only our algorithm can recover and enhance the standard distance candles that are the BHB stars (within the blue rectangle) and the

red clump (within the red rectangle), but even the MS is better characterized, with two almost parallel branches well-defined, corresponding to the Galactic disk and to the Galactic halo/Gaia-Enceladus-Sausage ([Haywood et al. 2018](#)). The only population for which our algorithm fails to improve the absolute magnitude prediction are the white dwarfs. This is due to a wrong estimation of the surface gravity for the white dwarfs by the SSPP, with  $\log(g) \simeq 5 \text{ cm s}^{-2}$  instead of  $\log(g) = 7-9 \text{ cm s}^{-2}$  (e.g. [Tremblay et al. 2013](#)). The precision of the spectro-photometric distances as function of the input spectroscopic parameters is discussed in Appendix B.

Once the ANN was trained, we applied it to all stars from the initial cross-match SEGUE-PS1-EDR3 catalogue. The catalogue composed of 308,692 stars with 13% precise distance will soon be available on VizieR.

### 2.3. Verification of the distance precision

Though the distances of MS stars are, by construction of our training sample, well established, this is not necessarily the case for the giants, where a doubt can persist regarding their precision. Here it is not possible to use globular clusters to perform an independent verification of the prediction of our algorithm due to the low number of globular cluster's stars observed by SEGUE that do not have their photometry affected significantly by crowding. However, a significant number of SEGUE stars are part of the Sagittarius (Sgr) stream, which covers a broad range of distances (e.g. [Koposov et al. 2012](#); [Belokurov et al. 2014](#)); we can therefore use this structure to verify the precision of our distances.

We identify stars member to the Sgr stream through their phase-space position (see Section 3). The residual contaminants are removed using the selection criteria based on proper motions and position on the sky described in [Ibata et al. \(2020\)](#). This leads to 888 SEGUE stars identified as part of the Sgr stream, mainly located between  $0^\circ < \text{R.A.} < 50^\circ$  and  $100^\circ < \text{R.A.} < 200^\circ$ , all of them being giant stars ( $\log(g) < 3.5$ ), either on the BHB or on the RGB.

To determine the DM variation along the Sgr stream, we use RR Lyrae stars, due to their small typical uncertainties on the distance, estimated to be 3% ([Hernitschek et al. 2018](#)). We applied the selection criteria of [Ibata et al. \(2020\)](#) on the position on the sky and proper motions on a catalogue of candidate RR Lyrae stars, built as the union of the *Gaia* DR2 SOS gaiadr2.vari\_rrlyrae ([Holl et al. 2018](#); [Collaboration et al. 2019](#); [Clementini et al. 2019](#)), the stars classified as RR Lyrae of a, b, c, d type in the general variability catalogues gaiadr2.vari\_classifier\_result, and the PS1 RR Lyrae of ab or cd type by ([Sesar et al. 2017](#))<sup>3</sup>. This leaves us with 10,384 potential Sagittarius stream RR Lyrae. The DM is determined assuming an absolute magnitude of  $M_G = 0.69$  mag, calculated from the  $M_G - [\text{Fe}/\text{H}]$  relation of [Muraveva et al. \(2018\)](#) for a mean metallicity of  $[\text{Fe}/\text{H}] = -1.3$  ([Ibata et al. 2020](#)). The variation of the Sgr distance modulus as a function of the position along the stream was determined by fitting a cubic spline to the RR Lyrae track (Fig. 3, top), where  $\Lambda_\odot$  is the longitude along the Sagittarius stream orbital plane ([Majewski et al. 2003](#)).

This DM track was then used to determine the expected absolute magnitude of the 888 SEGUE stars along the Sgr stream. The difference between this and the absolute magnitudes predicted by our method is shown in the lower panel of Fig. 3. The standard deviation is of 0.35 mag, larger than the 0.27 mag found

<sup>3</sup> With classification score above 0.6 and with a detection in *Gaia*.



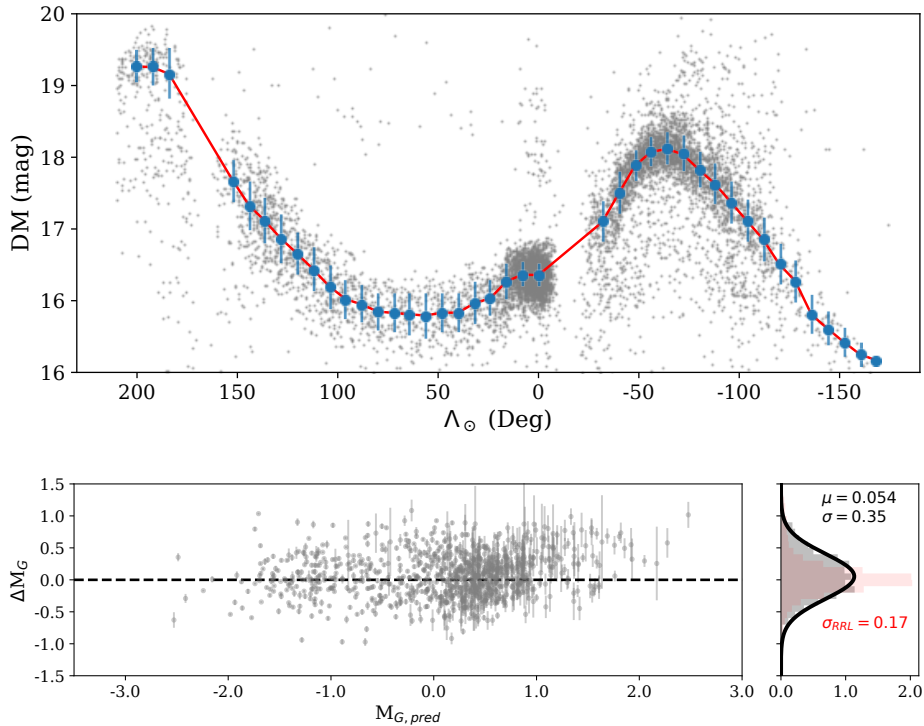


**Fig. 3.** *Top panel:* Distance modulus of the Sgr RR Lyrae as function of longitude along the plane of the Sagittarius stream, as defined by [Majewski et al. \(2003\)](#) (in grey). The blue error bars show the mean and standard deviation of the RR Lyrae DM as function of  $\Lambda_{\odot}$  position, and are used to define the Sgr DM track represented by the red cubic spline function. *Bottom panels:* Difference between the absolute magnitude derived by the distance modulus ridgeline and the absolute magnitude predicted by our algorithm as function of the predicted absolute magnitude for stars along the Sgr stream (left). On the right panel, the red histogram shows the normalized residuals of the distance modulus of the RR Lyrae to the fitted ridgeline along the Sgr stream.

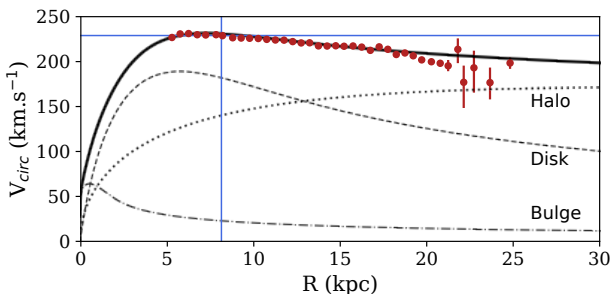


**Fig. 4.** Rotation curve of the Milky Way model used in this work (thick line) together with the measured rotation curve of our Galaxy by [Eilers et al. \(2019\)](#) (red dots). The thin blue lines show the rotation velocity at the Solar radius ( $229 \text{ km.s}^{-1}$  at  $8.129 \text{ kpc}$ ).

previously. However, this also includes the intrinsic width of the Sgr stream, as well as the scatter introduced by variations in the RR Lyrae metallicity and the  $M_G$ -[Fe/H] calibration itself. The dispersion of the Sagittarius stream RRL absolute magnitudes around the DM track amounts to  $0.17 \text{ mag}$  (red histogram in Fig. 3). By deconvolving the dispersion of the absolute magnitudes of SEGUE giants members to the Sagittarius stream with this value, we obtain  $0.31 \text{ mag}$ , leading to uncertainties on the distance of  $14\%$ , with a negligible bias of  $0.054 \text{ mag}$ ; this confirms the good accuracy of our algorithm. A  $14\%$  relative uncertainty on distance is probably an upper limit, since one can appreciate a small amount of contamination even after the position and proper motion cleaning, where this would lead to a

larger spread around the DM track. For the rest of the paper, we will continue assuming typical uncertainties of  $13\%$ .

We note that if we were to use an absolute magnitude of  $M_G = 0.64 \text{ mag}$  for the RR Lyrae stars as suggested by [Iorio & Belokurov \(2019\)](#) and [Vasiliev et al. \(2021\)](#), the dispersion in DM would not vary, but the bias would increase to  $0.097 \text{ mag}$ . It has to be noted here that the trend is similar for the BHBs and RGBs of the SEGUE sample. However, for the BHB, the Sgr DM variation that we fitted on the RRLyrae leads to a scatter on absolute magnitude of the BHBs of  $0.3 \text{ mag}$ , instead of the typical scatter of  $0.1 \text{ mag}$  found by [Deason et al. \(2011\)](#). This is again a consequence of scatter of the fitted DM variation on the RRLyrae, of the intrinsic scatter for the Sgr stream and of the uncertainties of our spectro-photometric distances estimation.

### 3. Scientific application: Exploration of the integral of motion-space

The catalogue of distances obtained in Sect. 2.2 enables the determination of the full 6 dynamical dimensions for a large number of distant stars having SEGUE spectroscopic and *Gaia* EDR3 proper motion measurements, without being restricted to a few specific stellar populations such as BHB, RC or RR Lyrae stars. This allows the exploration of the structures present in the outer disc-stellar halo integral of motion space (also called phase-space), similar to that recently conducted by [Naidu et al. \(2020\)](#) with the H3 survey ([Conroy et al. 2019b](#)). The integrals of motion are particularly useful to identify past accretion events, since the stars originating from the same object are still clustered

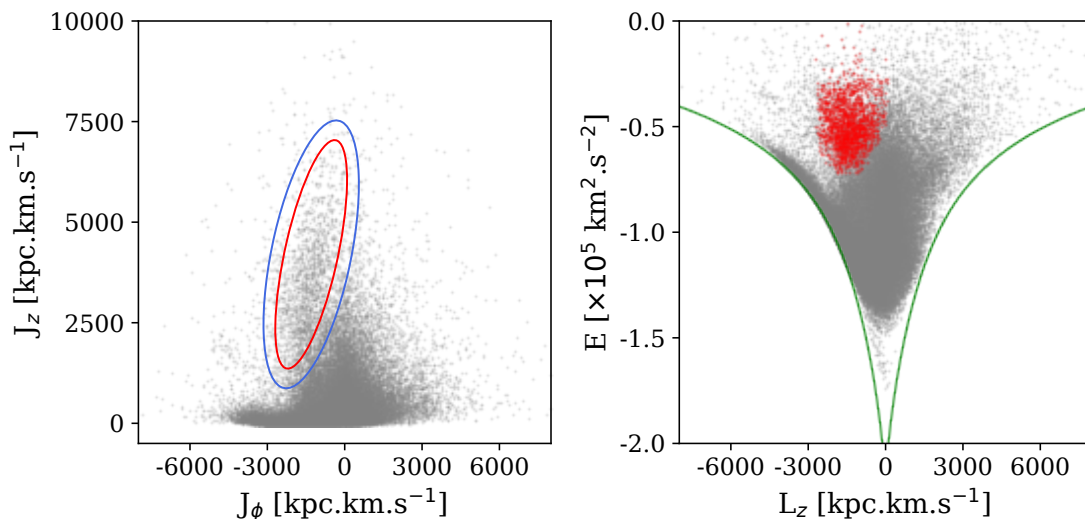


**Fig. 5.** Azimuthal and vertical actions of the stars from the SEGUE dataset (left), and corresponding energy-vertical angular momentum diagram (right). The green lines mark the locus of circular orbits in the Milky Way model. The red ellipse on the left panel shows structure clearly visible corresponding to the Sagittarius stream. The stars inside that selection are highlighted in red on the right panel. The stars between the red and blue ellipses in the left panel are used to estimate the background contamination, used in Fig. 6.

Disc	$\Sigma_0$ ( $M_\odot \cdot \text{kpc}^{-2}$ )	$R_d$ (kpc)	$z_d$ (kpc)	$R_m$ (kpc)
Thin	$1.4 \times 10^9$	2.3	0.18	0.0
Thick	$1.2 \times 10^8$	2.3	1.0	0.0
ISM	$2.2 \times 10^8$	4.6	0.04	4.6

Halo	$\rho_0$ ( $M_\odot \cdot \text{kpc}^{-3}$ )	$r_0$ (kpc)	$r_t$ (kpc)	q	$\gamma$	$\beta$
Bulge	$4.8 \times 10^8$	0.6	1.1	0.6	1.8	1.8
DM halo	$9.9 \times 10^6$	17.0	207	0.82	1	3

**Table 1.** Parameters of the GALPOT potential listed here, composed of 3 disc components corresponding to the thin and thick discs and the interstellar medium and 2 halo components corresponding to the bulge and the dark matter halo. The notation is the same than in Dehnen & Binney (1998).

in phase-space, even several Gyrs after the spatial coherence of the progenitor stellar component has been lost (Helmi & White 1999; Jean-Baptiste et al. 2016).

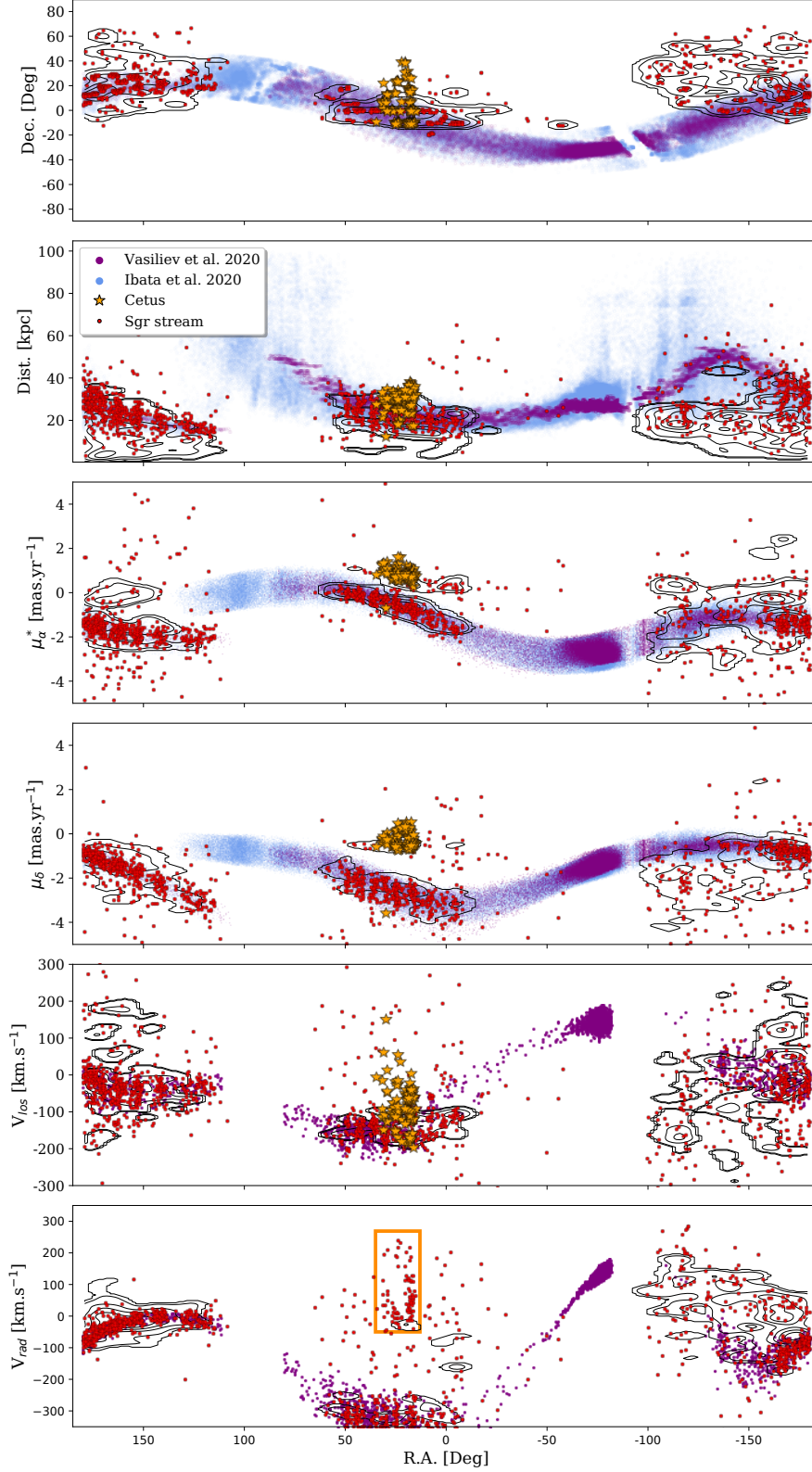
For the stars of the cross-matched SEGUE-PS1-EDR3 catalogue, we obtain the Cartesian Galactocentric positions and velocities, in a right-handed system, assuming that the circular velocity rotation at the Solar radius ( $R_\odot=8.129$  kpc,  $Z_\odot=20.4$  pc Gravity Collaboration et al. 2018) is  $v_0 = 229.0$  km.s $^{-1}$  (Eilers et al. 2019), with the Sun peculiar motions from Schönrich et al. (2010) ( $U_\odot, V_\odot, W_\odot$ ) = (11.1, 12.24, 7.25) km.s $^{-1}$ . The corresponding integral of motion quantities are computed using the Stäckel approximation method from the AGAMA python package (Vasiliev 2018). The potential used for this computation is based on the GALPOT potential (Dehnen & Binney 1998; McMillan 2017), composed of 3 exponential discs, representing the stellar thin and thick discs, the interstellar medium, the bulge, and the dark matter halo, whose parameters, listed in Table 2.3, have been tweaked to fit the rotation curve observed by Eilers et al. (2019), as shown on Figure 4.

Fig. 5 (left) shows the distribution of the azimuthal ( $J_\phi$ ) and vertical ( $J_z$ ) actions of the SEGUE stars. One can see a sub-structure around  $J_\phi \approx -3000$  kpc km s $^{-1}$ , at low  $J_z$ , which corresponds to the Galactic disc, as confirmed by the correspond-

ing position on the energy-vertical angular momentum<sup>4</sup> diagram (Fig. 5, right), close to a circular orbit (represented by the green line). In this last panel, one can also see a structure around  $L_z \sim 2000$  kpc.km.s $^{-1}$  and  $E \sim -0.7 \times 10^5$  km $^2$ .s $^{-2}$ , which corresponds to Sequoia (Myeong et al. 2018a,b, 2019). In addition to the disc, an elongated overdensity in the azimuthal and vertical action plane, highlighted by the red ellipse, is clearly visible (see the right panel of Fig. 5 for the stars location in E- $L_z$ ). The large majority of the stars forming this structure are part of the Sagittarius stream (Ibata et al. 1994), as it is visible in Fig. 6, where we compare their positions, heliocentric distance, proper motions, line-of-sight and Galactocentric radial velocities to those of the Sgr stream identified previously by Ibata et al. (2020) and Vasiliev et al. (2021).

However, as we can see from the different panels of Figure 6, aside from the Sgr stream, our action-space selection encompasses stars from the foreground/background (which includes other structures too, like the Gaia-Enceladus-Sausage, see Naidu et al. 2020) and a clear sub-structure at R.A. = 10 – 35°, which stands out in radial velocity and in the two proper motion components. To gauge the contribution of foreground/background, we overlay to Fig. 6 (shown by the black contour) the distribution of the stars lying at edge of the action-space selected area (i.e. be-

<sup>4</sup> The vertical angular momentum is equal to the azimuthal action in an asymmetric potential, as used here.



**Fig. 6.** Position on the sky, heliocentric distance, proper motions, line-of-sight and Galactocentric radial velocities of the stars from the structure that we identified in Fig. 5 (red symbols). The light blue and the purple points are the stars identified as part of the Sagittarius stream by [Ibata et al. \(2020\)](#) and [Vasiliev et al. \(2021\)](#) respectively. In the lower panel, another structure, highlighted by the orange rectangle, stands out around  $R.A. \sim 25^\circ$ , with stars having galactocentric radial velocity clearly distinct from the Sagittarius stream and from the background stars contamination (mostly originating from the Gaia-Enceladus-Sausage), shown by the black contours in each panels. The stars from this structure, that appears to be the Cetus stream, are shown by the orange stars in the other panels; they also form a distinctly visible structure in  $\mu_{\alpha,*}$  and  $\mu_{\delta,*}$ .



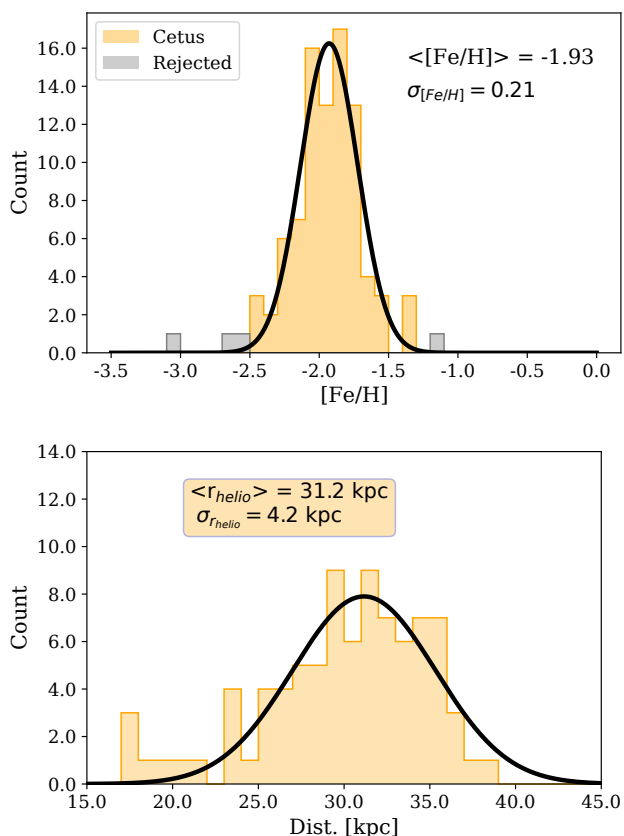


**Fig. 7.** *Upper panel:* Metallicity distribution of the Cetus stream spectroscopic sample. The grey histogram shows the metallicity of the 4 stars that were rejected by the sigma-clipping method. *Lower panel:* Distance distribution of the Cetus stream spectroscopic sample. The distribution is clearly asymmetric, with a tail toward shorter distances, which can be an indication of a distance gradient along the stream.

tween the red and blue ellipses on Fig. 5): here one can see stars mostly belonging to the Gaia-Enceladus-Sausage (see e.g. Naidu et al. 2020; Myeong et al. 2018c), but also a few stars with low  $J_z$  belonging to the Sgr stream not included in our ellipsoid selection. Nevertheless, the group of 91 stars between R.A. =  $10^\circ$ – $35^\circ$  and Galactocentric radial velocity between  $V_{rad} = -50$  and  $270$   $\text{km.s}^{-1}$  (within the orange box in the lower panel of Fig. 6 and highlighted with star symbols in the others) have a clearly different distribution from both that of the Sgr stream and the contamination. Comparing the position on the sky and the distances of those stars to previous works (Newberg et al. 2009; Koposov et al. 2012; Yam et al. 2013), we conclude that those stars are actually part of the Cetus stellar stream. We will refer to those stars as the "Cetus stream spectroscopic sample" in the rest of the paper.

Despite sharing similar position in energy, vertical and azimuthal actions, the spatial track of the Cetus stream differs from that of the Sgr stream by  $\sim 60^\circ$ , as already mentioned in these previous studies. This example clearly shows the limitation of the identification of stellar structures only on an energy-angular momentum diagram or in actions-space, without considering the action-angles, since it does not use the full 6 dimensional information available.

The metallicity distribution (obtained using the  $\text{FEHADOP}$  parameter) of the 91 stars in the Cetus stream spectroscopic sample is shown in the upper panel of Fig. 7. The mean metallicity is  $[\text{Fe}/\text{H}] = -1.93$  with a dispersion  $\sigma_{[\text{Fe}/\text{H}]} = 0.21$  dex, consis-

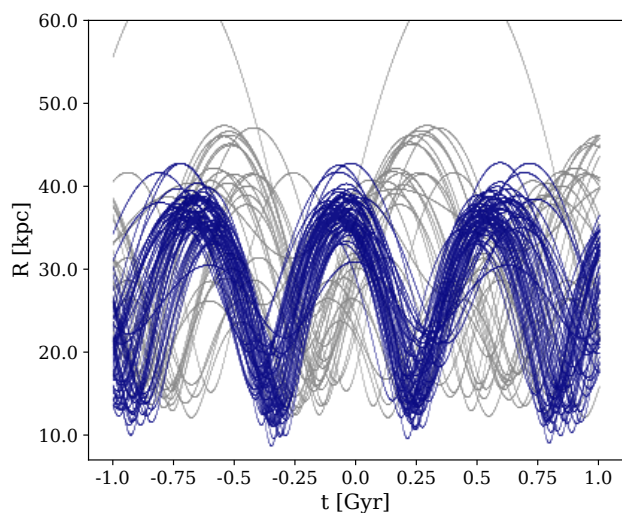


**Fig. 8.** Orbits of the Cetus stream spectroscopic sample stars integrated over 1 Gyr backward and forward. The blue orbits are the ones used to find the natural "coordinates" of the Cetus stellar stream.

tent with the values found by Yam et al. (2013) and Yuan et al. (2019). These values are insensitive to being derived from the full sample of 91 stars or by applying a  $3\text{-}\sigma$  clipping, which removes 4 stars.

The mean heliocentric distance we obtain for the Cetus stream spectroscopic sample is 31.2 kpc with a total dispersion of 4.2 kpc, including the distance uncertainties, consistent with previous measurements (Newberg et al. 2009; Koposov et al. 2012; Yam et al. 2013; Yuan et al. 2019) made in the same part of the sky, and with various stellar tracers (RGBs, BHBs and K-giants). However, the distance distribution (Fig. 7, lower panel) appears asymmetric, with a tail pointing toward shorter distances ( $\sim 20$  kpc), which could be an indication of a distance variation along the stream. Unfortunately, the spectroscopic Cetus sample is not sufficient to measure a distance gradient. In the next section, we expand the search for Cetus stream member stars using 5D information from *Gaia* EDR3 data.

#### 4. The Cetus stream in *Gaia* EDR3

In this section, we expand the search for Cetus member stars to the 5D *Gaia* EDR3 sample, in order to identify the edges of the stream, measure its distance gradient and estimate the stellar mass of its progenitor. To this aim, we will first use the 6D information from the Cetus stream spectroscopic sample to guide our search; specifically, we will be integrating the orbits of these stars to define the area of the sky likely to contain its tidal debris (Sect. 4.1). The search for Cetus stream member stars will be first carried out on BHB stars, whose absolute magnitude (and therefore distance) can be derived from photometric colours with good precision. For example, such relation exists for SDSS ( $g-r$ ) (Deason et al. 2011); since no such relation is currently available for the *Gaia* bands, and we do not want to be limited by the SDSS coverage, we first provide a re-calibration of the Deason et al. (2011) relation to the *Gaia* EDR3 photometric system (Sect. 4.2.1) and then use the likely BHBs identified in *Gaia* EDR3 data to analyse the Cetus stream, define its extent, distance gradient and track on the sky (Sect. 4.2.2). In Sect. 4.3, the properties derived in 4.2.2 are used to include stars in other evolutionary phases, assign probabilities of membership and estimate the mass of the progenitor.

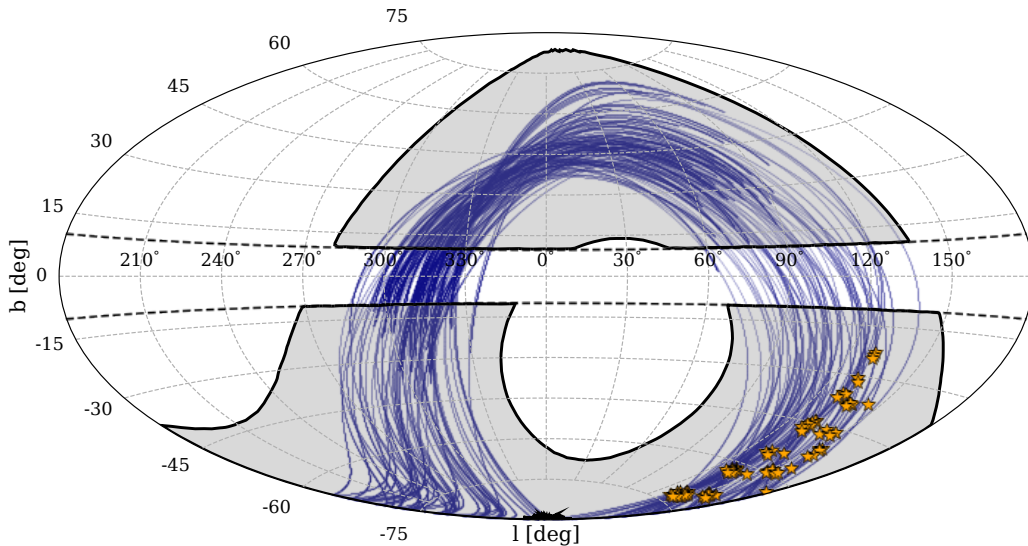


**Fig. 9.** Aitoff projection of the sky in Galactic coordinates; the area used to search for the Cetus stream is represented in grey. The region near the Galactic disc ( $|b| < 10^\circ$ ), within the dashed lines, is excluded from the search due to the high extinction and the large number of contaminant disc's stars. The blue lines correspond to the orbits of the stars from the Cetus spectroscopic sample used to find the plane of the Cetus stream. The current location of these stars is indicated by the orange stars.

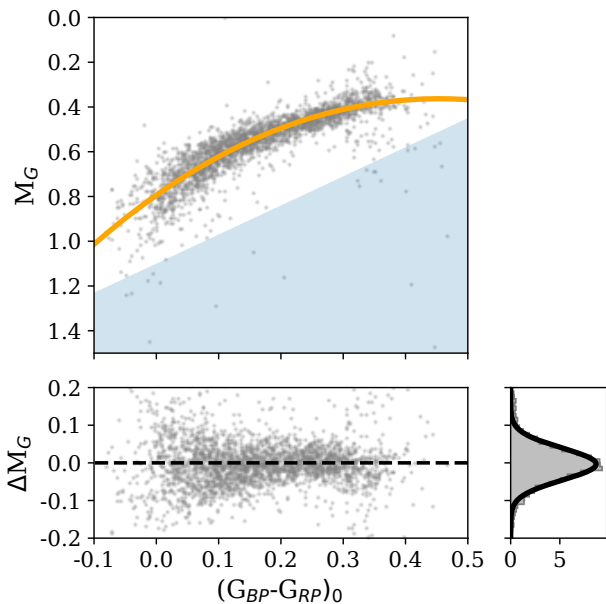


**Fig. 10.** Colour-absolute magnitude relation for BHB stars in the *Gaia* EDR3 photometric system. The orange line corresponds to the relation found in this work (Equation 1) by fitting a polynomial on the BHB population by [Xue et al. \(2011\)](#) (grey points). The stars in the blue area are excluded from the fit as they are likely misidentified as BHB. The lower panels show the residuals of the absolute magnitude to the fitted relation.

#### 4.1. The orbital plane of the Cetus stream

The track of stellar streams emanating from the disruption of globular clusters or small dwarf galaxies is well approximated by the orbital path of their progenitor (e.g. [Malhan & Ibata 2018](#) and [Ibata et al. 2021](#) used this method to detect new stellar streams in *Gaia* data). Recent simulations of [Chang et al. \(2020\)](#) show that the track of the Cetus stream follows quite well the orbit of its progenitor over 2 wraps, even if it originated from a dwarf

galaxy with a  $2 \times 10^9 M_\odot$  total mass. Therefore, it is possible to use the orbit of the stars of the Cetus stream spectroscopic sample to define its orbital plane, and thus the area of the sky where tidal debris are to be searched for.

The orbits were integrated backward and forward over 1 Gyr in the same MW potential used in the previous section. The variation in Galactocentric distance as a function of time is shown in Fig. 8. Over the 87 orbits, one star is clearly not related to the Cetus stream, with an apocenter completely different from all the others. The orbits of the majority of the other stars have a similar common behaviour (56/86, highlighted in blue in the figure), with a pericenter  $\sim 15$  kpc, an apocenter at  $\sim 37$  kpc, an orbital inclination of  $\sim 65^\circ$  and an orbital period of  $\simeq 600$  Myr, slightly lower than the value of 700 Myr found by [Yam et al. \(2013\)](#), betraying a more than probable common origin. Therefore, only one period forward and backward (i.e. between  $\pm 600$  Myr) of the 56 orbits with a common behaviour are used to define the orbital plane of the Cetus stream. The differences of most of the other 30 orbits to this common behaviour can be explained by the fact that these stars are not part of the Cetus stream. Indeed, the current galactocentric radial velocity of 14 of them exceeds  $150 \text{ km.s}^{-1}$ , contrary to the stars showing a common orbital behaviour, whose galactocentric radial velocities ranges from 0 to  $150 \text{ km.s}^{-1}$ . For 10 others, the current distance ranges between 18 kpc and 25 kpc, while the current distance of the stars with a common orbital behaviour is between 25 kpc and 40 kpc. For the 6 others the deviating orbital behaviour could be a consequence of the combined uncertainties on the observables (PMs, distance and radial velocity). Note that it is also possible that the departure from the common behaviour of all these stars is caused by the simple assumption we made that the Cetus stream is a fully coherent structure, disrupted in an adiabatic process, which neglects for example the perturbations generated by a massive LMC. Interestingly, removing those 30 stars does not change the mean metallicity we found for the Cetus stream of  $[\text{Fe}/\text{H}] = -1.93 \pm 0.21$ , while the mean heliocentric distance increases slightly and the dispersion is reduced (from 31.2 to 32.0 kpc and from 4.2 to 2.8 kpc, respectively).

Although usually the "natural" coordinates of a stellar stream are expressed using a great circle rotation (i.e. [Ibata et al. 2001](#); [Koposov et al. 2010, 2019](#); [Shipp et al. 2019](#)), in the case of the Cetus stream, we found that a small circle is better suited. Indeed, in a Galactocentric frame, the projected coordinates will follow a great circle, but this is not the case anymore if the observer is located on Earth, and a constant offset is visible in the coordinate perpendicular to the stream. We found that the "natural" coordinates of the Cetus stream ( $\phi_1, \phi_2$ ) are well expressed by a small circle with a pole centred on (R.A., Decl.)=(125.1809832°, 15.91290743°) and an offset to the great circle of 14.36°. The transformation of coordinates is performed with the `GREATCIRCLEICRSFRAME` class present in the `GALA` package ([Price-Whelan 2017](#)), with  $\phi_1, \phi_2$ =(0,0) corresponding to (R.A., Decl.)=(22.11454259°, -6.7038421°), where we think the centre of the progenitor of the Cetus stream is located (see Section 4.2.2).

Hereafter, we limit the search of stars belonging to the Cetus stream to the region between  $|\phi_2| < 35^\circ$ , since it contains the 56 orbits used to define the stream orbital plane. Moreover, we exclude the region at  $|b| < 10^\circ$  due to the high extinction and the large number of disc's stars. The corresponding search area is highlighted in grey in Fig. 9.

#### 4.2. Tracing the Cetus stream with BHB stars

Blue horizontal Branch (BHB) stars are very often used to estimate the distance of sub-structures since they are relatively bright stars and their absolute magnitude is, to a first approximation, constant ( $M_g \sim 0.5$  in the SDSS  $g$ -band; [Deason et al. 2011](#)). Therefore, we first use this stellar population to investigate the extent of the Cetus stellar stream and to measure the distance gradient along it.

##### 4.2.1. BHBs distance calibrated for *Gaia* EDR3

[Deason et al. \(2011\)](#) found that the absolute magnitude of BHB stars, and so their heliocentric distances, is a function of their colour, with a narrow scatter around the relation they derived ( $\sim 0.1$  mag). This relation was calibrated for the SDSS photometric system; however, SDSS only covers a fraction of the orbital plane of the Cetus stream. In order to exploit the full sky coverage afforded by *Gaia*, we re-calibrate the [Deason et al. \(2011\)](#) relation in the *Gaia* EDR3 photometric system.

To this aim, we used the sample of BHBs identified spectroscopically by [Xue et al. \(2008\)](#) in SEGUE, adopt their SDSS photometry to derive their distance modulus using the relation by [Deason et al. \(2011\)](#), and use it to compute their absolute magnitude in the *Gaia*  $G$ -band,  $M_{G,BHB}$ . As shown in Fig. 10,  $M_{G,BHB}$  can be expressed as:

$$M_{G,BHB} = -0.266(G_{BP} - G_{RP})_0^3 + 2.335(G_{BP} - G_{RP})_0^2 - 1.955(G_{BP} - G_{RP})_0 + 0.794. \quad (1)$$

Here we have excluded the stars with  $M_G > -1.3(G_{BP} - G_{RP})_0 + 1.1$ , since they are clearly deviating from the general trend, possibly because the [Xue et al. \(2008\)](#) BHB sample is not 100% pure (see [Starkenburger et al. 2019](#)). It has to be noted that 2, 160 stars of the 2, 362 used are located in the range of validity of the [Deason et al. \(2011\)](#) relation, i.e.  $-0.25 \leq (g - r)_0 \leq 0.0$ .

The scatter between the absolute magnitude estimated by our re-calibration and that by [Deason et al. \(2011\)](#) is  $\sigma_{\Delta M_G} = 0.04$  mag, smaller than the intrinsic precision of 0.1 mag of the [Deason et al. \(2011\)](#) relation, and with a negligible offset ( $< 0.005$

mag). This means that our method has a relative distance precision similar to the [Deason et al. \(2011\)](#) calibration, i.e. 5%.

##### 4.2.2. Identification of BHB candidates along the Cetus stream

In order to search for BHB candidates along the Cetus stream, we selected *Gaia* EDR3 sources with  $G_{BP}-G_{RP})_0 \leq 0.5$  located in the plane of the Cetus stream ( $|\phi_2| < 35^\circ$ ). We removed sources that had either the duplicate flag on, a spurious astrometric solution (with the Re-normalised Unit Weight Error, RUWE  $> 1.4$ , Lindegren, document GAIA-C3-TN-LU-L-124-01), located in high-extinction areas ( $E(B-V) > 0.3$ ) or with high uncertainties on their parallax measurement ( $\varpi > 0.4$  mas).

Since the Cetus stream has a pericenter of  $\sim 10$  kpc (Fig. 8), we applied a generous cut on the parallax such that stars with  $\varpi - 3\delta\varpi < 1/5$  mas are kept; this removes a large portion of disc contamination.

To limit contamination, we also removed stars located within: 15x the half-light radius of any globular clusters around the MW (using the values given by [Harris 2010](#)); 5x the half-light radius of the dwarf galaxies listed in the catalogue of [McConnachie \(2012\)](#), an ellipse centred on M31 with a semi-major axis of  $3^\circ$  and a semi-minor axis of  $1.5^\circ$  oriented of  $38^\circ$  ([de Vaucouleurs 1958](#)) and within the inner  $1^\circ$  of M33; an ellipse centred on the LMC with semi-major/minor axis of  $26^\circ$  and  $11.6^\circ$  respectively, and in an ellipse centred on the SMC with a semi-major axis of  $20^\circ$  and a semi-minor axis of  $8^\circ$ . For M31, M33, LMC, SMC, these values have been chosen by visual inspection.

The distance distribution of the selected blue point-sources is shown in Fig. 11 a) as a function of longitude along the Cetus stream orbital plane,  $\phi_1$ . These contain not only BHB stars, but also contamination from blue straggler (BS), white dwarf (WD), young main-sequence turn-off stars (y-MSTO), as well as distant quasi-stellar objects (QSO) (e.g. [Sirko et al. 2004](#); [Vickers et al. 2012](#); [Fukushima et al. 2018](#)). We removed the known QSOs compiled by [Liao et al. \(2019\)](#). As for removing the majority of the stellar contaminants, we perform a series of gradually more restrictive kinematic selections. Such a process allows in a first step to detect the full extent of the stream, without cutting its edges by performing a very restrictive selection, and then to clean the sample in a second step.

Stars in a stream generally do not have large motions in the direction perpendicular to the orbit, unless there are strong perturbers (e.g. [Erkal et al. 2019](#)), and have a common direction of movement, parallel to the orbit. For these reasons, based on the orbits of the Cetus stream spectroscopic sample, we perform a first broad kinematic selection, visible in Fig. 11 e), such as ( $\mu_{\phi_1,corr} < 0.0$  mas.yr $^{-1}$  and  $-1.3$  mas.yr $^{-1} < \mu_{\phi_2,corr} < 1.8$  mas.yr $^{-1}$ ), where  $\mu_{\phi_1,corr}$  and  $\mu_{\phi_2,corr}$  are the proper motions along the Cetus coordinates, corrected for the Sun reflex motion, using the individual distances estimated from Equation 1 and the solar motion used in Section 3. As visible on Fig. 11 b), we can already clearly identify the stream structure between  $-40^\circ < \phi_1 < 40^\circ$ . This wide generous selection still includes contamination, such as background/foreground BHBs from the Galactic discs and stellar halo, as well as blue stars misidentified as BHBs.

Since distances (and corrected proper-motions) for misidentified BHBs will be incorrect, we also look into non-corrected proper motions. Based on the orbits of the stars derived earlier, we see that a second broad selection keeping stars with  $3.3$  mas.yr $^{-1} > \mu_{phi,2} > 0.04 \cdot \phi_2 - 0.9$  mas.yr $^{-1}$ , as shown



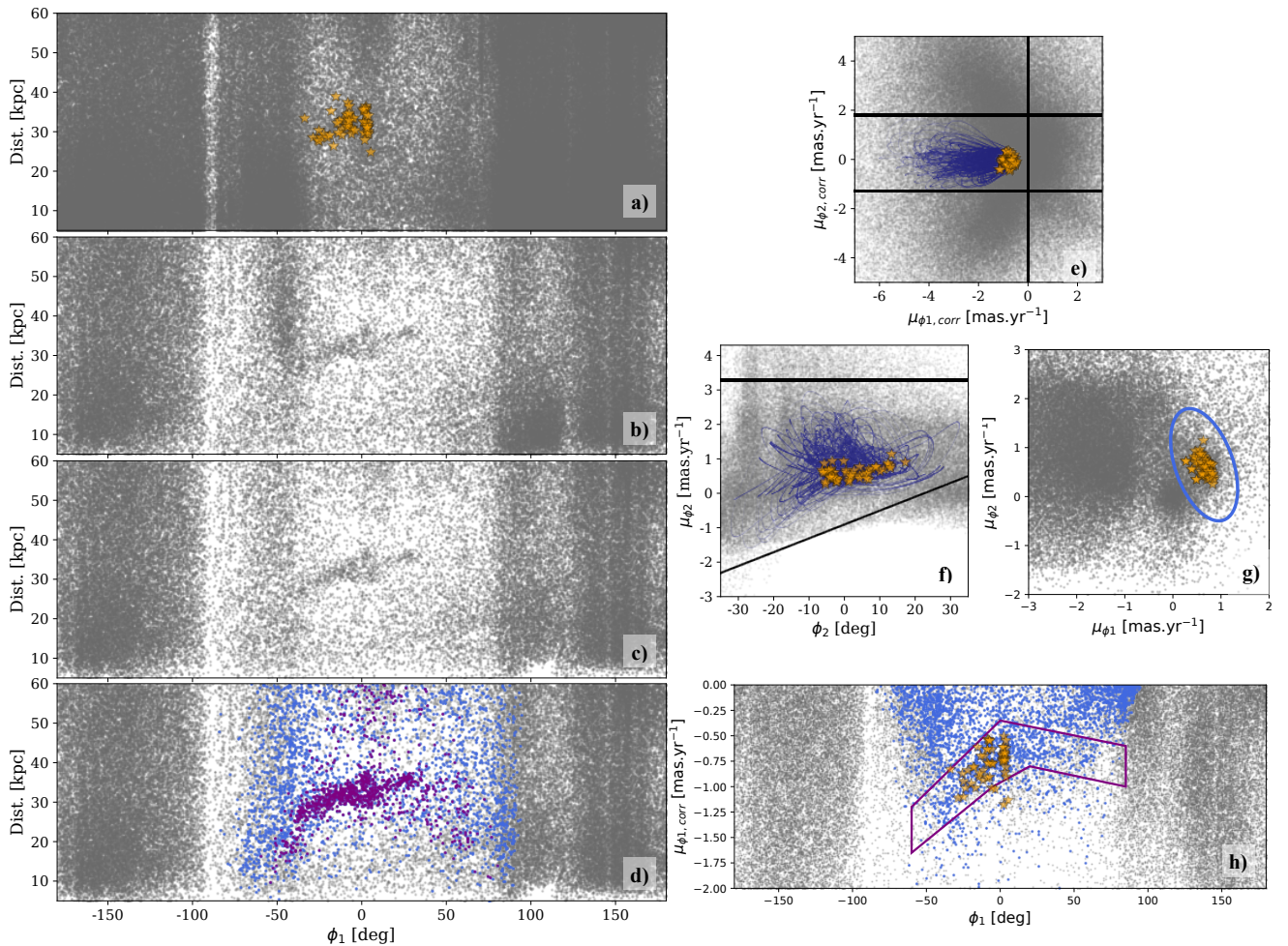


**Fig. 11.** *Panel a)* shows the distance distribution of BHB stars, prior to any kinematic selections, where the orange stars show the position of the 56 spectroscopic stars whose orbits have been used to define the orbital plane of the Cetus stream. *Panel b)* shows the same distribution for stars after a first broad kinematic cut performed in the corrected proper motion, illustrated by the black lines in *panel e)*, where the blue lines show the orbits of the spectroscopic stars, used to define this cut. *panel c)* shows the distance distribution of BHB stars after an additional wide selection based on their non-corrected proper motions, as shown in *panel f)* (see Section 4.2.1). The *panel d)* shows the distribution of the BHBs of the Cetus stream (in purple) after 2 additional more restrictive selections to remove the contamination of foreground/background stars performed in the non-corrected proper motion space, shown in *panel g)* and in the position-corrected parallel proper motion space, shown in *panel h)*. In all panels,  $\phi_1$  and  $\phi_2$  refer to the "natural" coordinates of the Cetus stream (see Section 4.1).

in Fig. 11 f) removes a small fraction ( $\approx 16\%$ ) of the sample, but improves the detection of the edges of the stream around  $\phi_1 \approx \pm 50^\circ$  (Fig. 11 c). In equatorial coordinates, this region corresponds to an area located between  $-10^\circ \lesssim \text{R.A.} \lesssim 50^\circ$  and  $-90^\circ \lesssim \text{Decl.} \lesssim 55^\circ$ , extending the previous detection of the Cetus stream (Newberg et al. 2009; Yam et al. 2013; Yuan et al. 2019) over several tens of degrees in the equatorial Southern Hemisphere, overlapping with the position of the Palca overdensity discovered by Shipp et al. (2018), as predicted recently by Chang et al. (2020). Therefore, to avoid future confusions, we propose to rename the stream as the "Cetus-Palca stream".

However, neither in Fig. 11 b) nor c), we see the trace of the northern (galactic) counterpart detected by Yuan et al. (2019) in phase-space, which should be located around  $\phi_1 \sim 150^\circ$  ( $l \sim 50^\circ$ ,  $b \sim 50^\circ$ ). The detection of clear edges to the Cetus-Palca stream, and the absence of broadening toward them in Fig. 11 c) may suggest that the northern detection of Yuan et al. (2019) is an artefact, or not related to the Cetus-Palca stream. However, this northern counterpart is expected to be spatially diffuse, and

it may not appear as a structure distinguishable from the background/foreground in our selection.

To clean out the broadly selected sample, we applied two more restrictive selections, once again in kinematic space, since selecting in position and distance spaces could let to cut the stream before its actual edges. The first cut, was done in (non-corrected) proper-motion space, as the Cetus-Palca stream stands out from most of the Milky Way contaminants, as highlighted by the blue ellipse in Fig. 11 g). The stars within this ellipse are indicated by the blue points in Fig. 11 d) and f). Since this sample still contains a large amount of contaminants, mostly from the disc, we look at the position-parallel proper motion space (Fig. 11 h) to select the BHB stars part of the same structure as the stars from the spectroscopic sample. The final cleaned sample of BHBs stars part of the Cetus-Palca stream is shown in purple in Fig. 11 e). We can clearly see the Cetus-Palca stream between  $-40^\circ \leq \phi_1 \leq 35^\circ$ . Around  $\phi_1 = 0^\circ$ , the stream appears wider compared to the other sections, which could indicate the position where the leading and trailing arms meet, and so where the progenitor should be, if it was not completely disrupted. This

motivated our choice for the location of the origin of the  $\phi_1$  axis in Sect. 4.1.

With the final BHB selection, one can see a clean, almost linear, distance gradient along the Cetus-Palca stream, with a distance varying between  $\sim 25$  kpc at the edge of the leading arm ( $\phi_1 \approx -40^\circ$ ) to  $\sim 37$  kpc at the edge of the trailing arm ( $\phi_1 \approx 35^\circ$ ). This explains the asymmetric distribution in the distance found with the Cetus-Palca stream spectroscopic sample, since SEGUE covers only the leading arm ( $\phi_1 < 0^\circ$ ) of the Cetus-Palca stream.

#### 4.3. Tracing the Cetus-Palca stream with different stellar populations

As said in the previous section, BHB stars are perfect to trace the position and the distance gradient along the Cetus-Palca stream. However, these stars only represent a small fraction of the total number of stars of, either a dwarf galaxy or a globular cluster, which make them unpractical to measure the stellar mass of an object like Cetus-Palca. Therefore, to explore further the properties of the Cetus-Palca stream, we expand the analysis also to other stellar populations. For this analysis, we used the information gained in the previous section to select potential members of Cetus-Palca.

The initial selection of stars is similar to that done for the BHBs, except that the colour selection criteria is broader, with  $-0.5 \leq (G_{BP}-G_{RP})_0 \leq 1.7$ . Moreover, we restricted the analysis to  $-75^\circ < \phi_1 < 75^\circ$  and to stars with  $\varpi > -0.4$  mas. Since we found that Cetus-Palca is always located at distance farther than 20 kpc, we imposed that all stars should have  $\varpi < 1/5$  mas (rather than  $\varpi - 3\delta\varpi < 1/5$  mas for the BHBs), again, in the optic to remove stars very likely from the disc, while keeping the larger number of stars of the halo as possible. Finally, we restrict the analysis to the proper motion plane  $-3 \text{ mas.yr}^{-1} \leq \mu_{\phi,1} \leq 2 \text{ mas.yr}^{-1}$  and  $-2 \text{ mas.yr}^{-1} \leq \mu_{\phi,2} \leq 3 \text{ mas.yr}^{-1}$ .

Our adopted approach to select stars likely members of the Cetus-Palca stream is largely inspired by the methods used to discriminate statistically the stars of a dwarf galaxy from the background/foreground contamination (e.g. Martin et al. 2013; Longeard et al. 2018; Pace & Li 2019; McConnachie & Venn 2020a,b; Battaglia et al. 2021). The general idea behind those methods is that for any star in *Gaia*, it is either a member of a stellar structure (e.g. a dwarf galaxy or a stellar stream) or of the Milky Way foreground/background. Therefore, the un-marginalised likelihood  $\mathcal{L}$  of a given star can be defined such:

$$\mathcal{L} = f_{sub} \mathcal{L}_{sub} + (1 - f_{sub}) \mathcal{L}_{MW} , \quad (2)$$

where  $\mathcal{L}_{sub}$  and  $\mathcal{L}_{MW}$  are respectively the likelihoods of the stellar sub-structure and of the MW foreground/background, and  $f_{sub}$  is the fraction of stars in the stellar structure.

$\mathcal{L}_{sub}$  and  $\mathcal{L}_{MW}$  can be decomposed as a spatial ( $\mathcal{L}_s$ ) and a kinematic ( $\mathcal{L}_{PM}$ ) components. However, contrary to dwarf galaxies that cover a small area of the sky and for which there is no spatial variation of the measured proper motions (at the first order and with the current precision of the instrument), this is not the case for an elongated stellar stream such as Cetus-Palca. Similarly, the proper motions of the MW stars vary strongly with position on the sky. Therefore, we decoupled the kinematic component in two terms, where the first one  $\mathcal{L}_{PM1}$  is the likelihood of the proper motion at a given position along the first axis, and  $\mathcal{L}_{PM2}$  is the likelihood of the proper motion at a given position along a second perpendicular axis. As the result,  $\mathcal{L}_{sub}$  and  $\mathcal{L}_{MW}$

are expressed as:

$$\mathcal{L}_x = \mathcal{L}_{s,x} \mathcal{L}_{PM1,x} \mathcal{L}_{PM2,x} , \quad (3)$$

where the index  $x$  refers either to the MW or to the satellite. Contrary to the works mentioned previously, we did not use colour-magnitude information to compute the probability to be a member of Cetus-Palca since we wanted to use it as an independent validation check of our method, but also because we used the luminosity function to measure the stellar mass of Cetus-Palca.

For this analysis, we worked with the equatorial coordinates, both for position and proper motions, (R.A., Dec.,  $\mu_\alpha^*$  and  $\mu_\delta$ ) because we can assume, in a first approximation, that the variation of  $\mu_\alpha^*$  along the right ascension axis is decoupled from the variation of  $\mu_\delta$  along the declination axis. This is not the case if we were working in the Cetus-Palca coordinates, since we would have to introduce a correlation matrix for the proper motion perpendicular to the plane of the stream ( $\mu_{\phi_2}$ ) to include its variation along  $\phi_1$  and along  $\phi_2$ .

For the stream likelihood ( $\mathcal{L}_{sub}$ ), the positional proper motion likelihoods in the right ascension and declination planes  $\mathcal{L}_{PM1,sat}$  and  $\mathcal{L}_{PM2,sat}$  are computed from the BHBs identified as being part of the Cetus-Palca (see Section 4.2.2). For both planes, we modelled the variation of the proper motion with the position by a 3-order polynomial fitted on the distribution of the Cetus-Palca BHBs. Then, at every position, the distribution of proper motion is modelled by a Gaussian function with a width equal to the residual BHB distribution with respect to the polynomial fit ( $\sigma = 0.197 \text{ mas.yr}^{-1}$  for the right ascension plane and  $\sigma = 0.143 \text{ mas.yr}^{-1}$  for the declination plane). Since it has been found in previous works that the morphology of the Cetus-Palca stream is rather complex (Newberg et al. 2009; Yam et al. 2013; Yuan et al. 2019), and because the foreground/background MW contamination is largely dominating the signal, we assumed a uniform distribution for the spatial likelihood for the stream.

For the MW foreground/background distribution, because it largely dominates the signal, we constructed the spatial and the two kinematics likelihood components directly from the distribution of the selected *Gaia* stars, and smoothed it over  $1^\circ$  spatially and over  $0.05 \text{ mas.yr}^{-1}$  in proper motion space.

The fraction of stars part of Cetus-Palca ( $f_{sub}$ ) was found by exploring the parameters space of the posterior distribution with EMCEE (Foreman-Mackey et al. 2013). The posterior distribution of the data ( $D$ ), given a model with a fraction of stars in Cetus-Palca  $f_{sub}$ , is defined such as  $P(D|f_{sub}) \propto \mathcal{L} \times P(f_{sub})$ , where  $P(f_{sub})$  is a uniform flat prior on  $f_{sub}$  between 0 and 1. Doing so, we found a fraction of stars in Cetus-Palca equal to  $f_{sub} = 0.00837 \pm 0.00016$ .

Once the value of  $f_{sub}$  is found, it is possible to compute the probability of each star to be part of Cetus-Palca ( $P_{Cetus}$ ) such as:

$$P_{Cetus} = \frac{f_{sub} \mathcal{L}_{sub}}{f_{sub} \mathcal{L}_{sub} + (1 - f_{sub}) \mathcal{L}_{MW}} . \quad (4)$$

The spatial distribution of the 17,990 stars with  $P_{Cetus} \geq 0.2$  is shown in the lower panel of Fig. 12. The selection stills contains contamination from the MW disk, from the LMC and from the Sgr stream. However, we can clearly see on the bottom panel the extent of the Cetus-Palca stream, whose position is highlighted by the blue rectangle on the upper panel. We divided arbitrarily the stream in 7 boxes of equal area, for which we present the respective colour-magnitude diagrams in Fig. 13. The red giant branch of the Cetus-Palca stream is clearly visible in each of these boxes, and has a very different signature than the



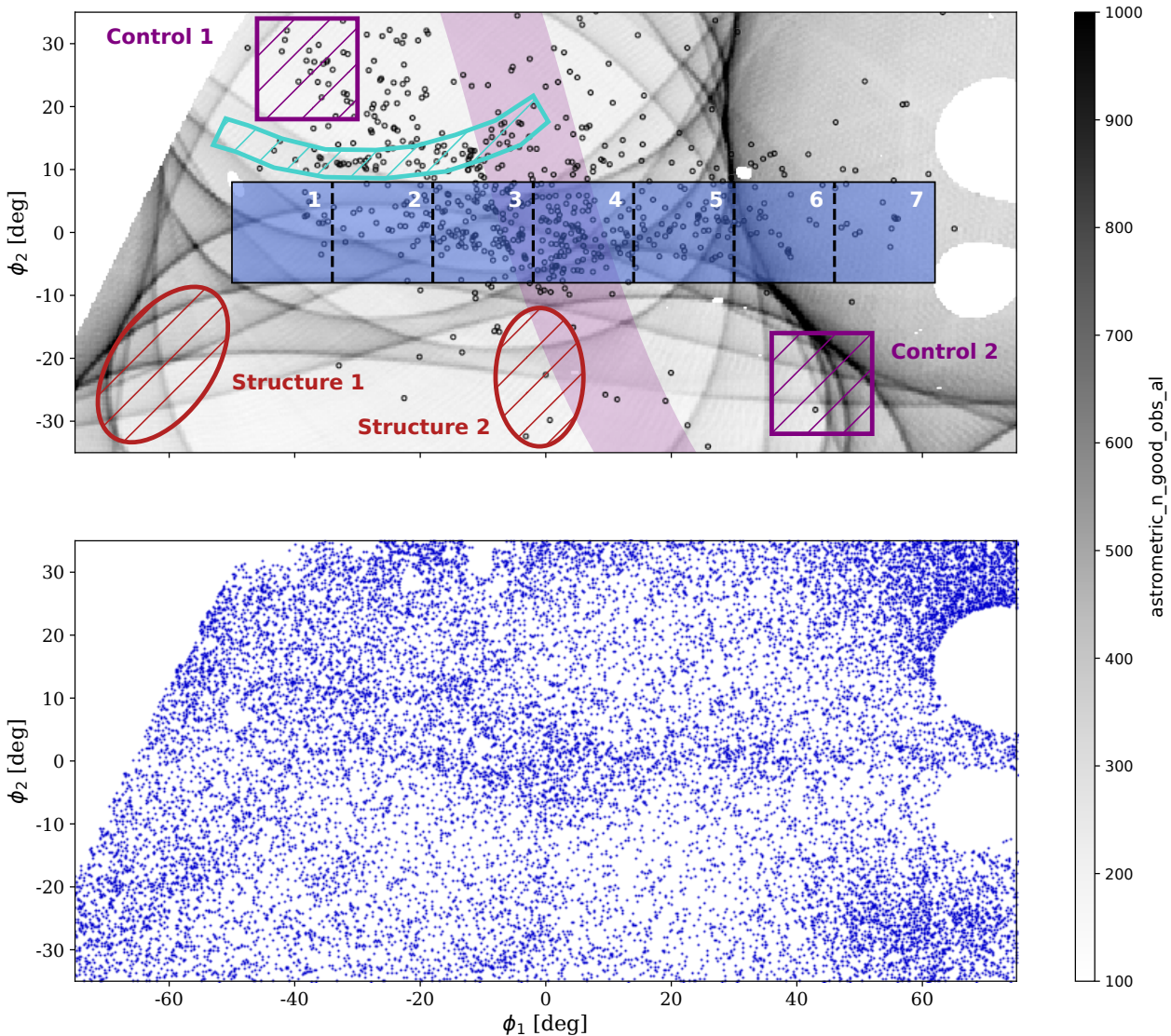


**Fig. 12.** *Lower panel:* position of the stars with  $P_{Cetus} \geq 0.2$ . *Upper panel:* The black circles show the position of the BHB of Cetus-Palca identified in Section 4.2.2, and the yellow stars show the position of the 56 stars of the Cetus-Palca spectroscopic sample with common orbital behaviour. The blue rectangle highlights the position of the Cetus-Palca stream visible in the lower panel. The stream is decomposed in 7 boxes of equal area, used to measure the spatial variation of the CMDs in Fig. 13. The cyan polygon highlights the position of the potential globular cluster stream that we found in this work. The two purple dashed rectangles highlight the region located outside the Cetus-Palca stream used to show the MW foreground/background CMD. The red dashed ellipses show the position of two additional structures visible in the lower panel. The light purple band shows the track of the Sgr stream. Finally, the black and white 2D histogram in the background shows the number of good observations along the scan direction of *Gaia* (ASTROMETRIC\_N\_GOOD\_OBS\_AL).

background, as shown by the CMDs of the 2 control areas (purple rectangle in Fig. 12). The CMDs of Boxes 3 and 4 are by far the most populated. These two boxes cover the region where we hypothesize the center of the progenitor is (Section 4.2.2). For each box, we manually adjusted the distance modulus (DM) of a 14 Gyr MIST isochrone with  $[\text{Fe}/\text{H}] = -1.93$  (Dotter 2016; Choi et al. 2016) to the CMD. The age of the isochrone was chosen because it gives the best fit to the colour extent of the BHBs, and the metallicity corresponds to that we measured with the spectroscopic sample (Section 5). The variation of distance thus measured is well consistent with that measured from the BHBs.

The co-added CMD of the 7 boxes where was identified Cetus-Palca is shown in panel a) of Fig. 14, with overlaid an

MIST isochrone with a distance modulus of 17.7 mag. To take into account the variation of distance along the Cetus-Palca stream, before co-addition, the various CMDs were offset by the difference of the distance modulus indicated in each panels of Figure 13 to mean distance modulus of Cetus-Palca of 17.7 mag. The red giant and blue horizontal branches are clearly visible, while the contamination from MW stars is relatively low, since the disc main-sequence is barely detectable. On this figure, the black presents the RGB selection box whose luminosity function is shown in panel b). We compared the luminosity function of the observed RGB to a fiducial RGB population with a Kroupa (2001) mass distribution to adjust the total luminous mass of Cetus-Palca. For this, we only used the stars



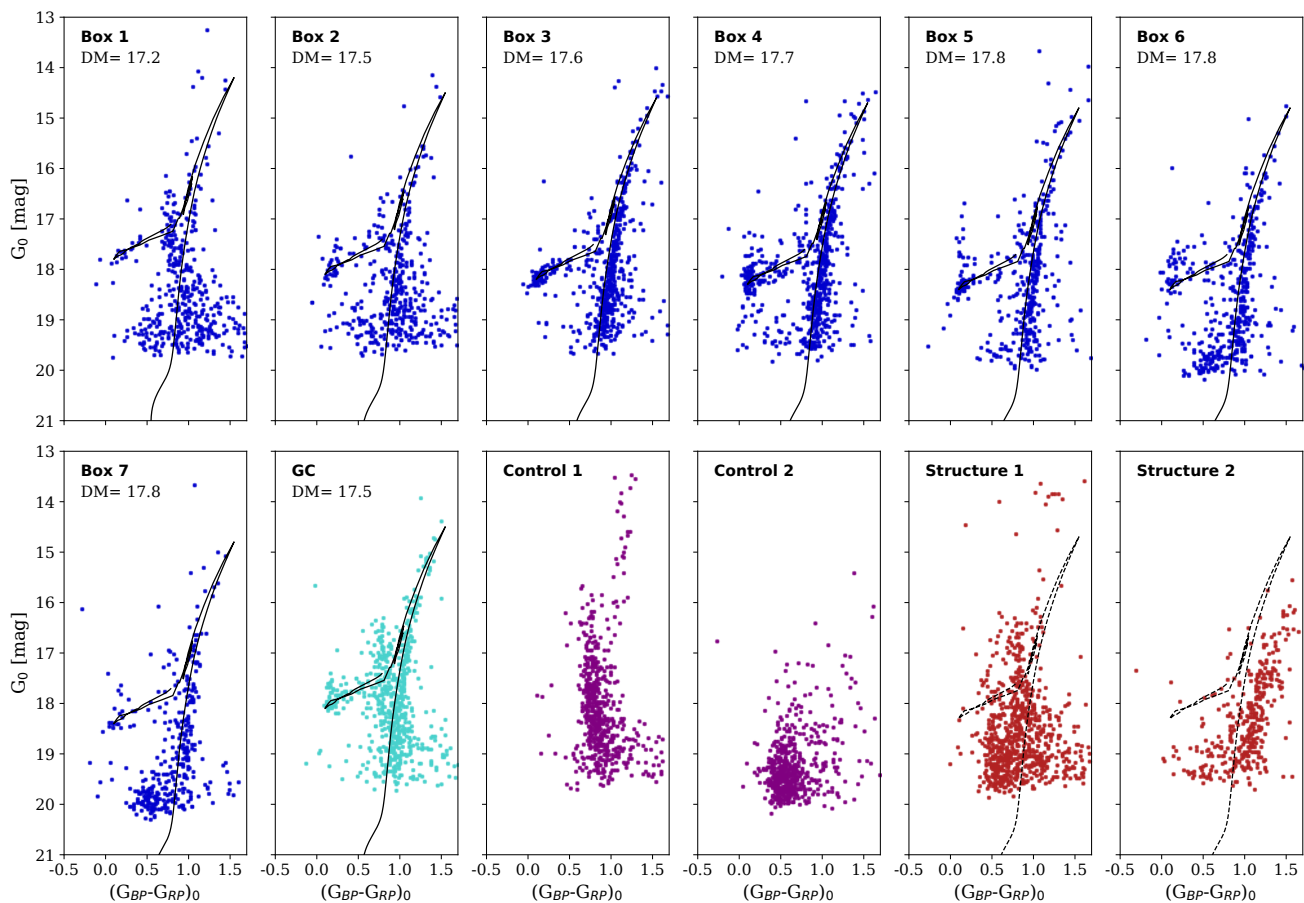


**Fig. 13.** Color-magnitude diagrams of the different spatial regions shown in Fig. 12 in which the black line shows a MIST fiducial isochrone for a 14 Gyr old population with a metallicity of  $[\text{Fe}/\text{H}]=-1.93$ , shifted by the distance modulus (DM) indicated in the legends. For Structure 1 and 2, the distance modulus is of  $\text{DM}=17.7$ . The colours of the symbols reflects the color-coding of the structures highlighted in Fig. 12.

brighter than  $G_0 = 18.5$ , since the completeness drops rapidly at fainter magnitudes. This corresponds to the threshold magnitude up to which *Gaia* can be considered as complete in this region of the sky (Boubert & Everall 2020). We performed 100 random realizations to take into account the photometric uncertainties of each star. Doing so, we found that the resulting stellar mass ranges between  $1.3-1.6 \times 10^6 M_\odot$ , with a median of  $1.4 \times 10^6 M_\odot$ , consistent with the upper mass range found by Yuan et al. (2019). If we were to consider stars with  $P_{\text{Cetus}} \geq 0.1$ , we would obtain a very similar result, with a stellar mass between  $1.3-1.7 \times 10^6 M_\odot$ . This is in the same order of magnitude than "classical" dwarf spheroidal galaxies like Sextans or Sculptor, which have a stellar mass of  $0.4 \times 10^6$  and  $7.8 \times 10^6 M_\odot$ , respectively (Irwin & Hatzidimitriou 1995; Lokas 2009; de Boer et al. 2012). According to the stellar mass-metallicity relation for Local Group dwarf galaxies from Kirby et al. (2013), such a massive galaxy should have a metallicity of  $[\text{Fe}/\text{H}]=-1.63 \pm 0.16$ . This is consistent with the metallicity that we measured for the Cetus-Palca stream in Section 3, though it is in the lower edge of the observed stellar mass-metallicity relation by Kirby et al. (2013). However, this relation has large uncertainties in the metal-poor regime, and a galaxy with a similar stellar mass, namely Andromeda III, is also found to be more metal poor than predicted by this relation, with  $[\text{Fe}/\text{H}]=-1.84 \pm 0.05$  (Kirby et al. 2013).

#### 4.4. Detection of a potential stream of stream

In addition to the Cetus-Palca stream, another, fainter, stream-like structure parallel to the Cetus-Palca stream, located around  $\phi_2 \approx 10^\circ$ , is visible in Fig. 12 (highlighted by the cyan polygon on the upper panel). This structure is also visible in the distribution of the BHBs we identified as member of Cetus-Palca (black circles in the upper panel of Fig. 12). The position of this structure does not coincide with an area observed more than others by *Gaia* and where the completeness could be higher, as illustrated by the number of good observations in the along-scan direction of the *Gaia* satellite, `ASTROMETRIC_N_GOOD_OBS_AL`, (2D histogram in the upper panel of Fig. 12). This structure seems to be spatially decoupled from the position of the Cetus-Palca stream and the CMD of the stars in that region (whose area is equal to what of an individual box along Cetus-Palca) is more populated than in any of the neighboring boxes.

The small width of this stream ( $\approx 300$  pc) could indicate that it might be formed by the tidal debris of a disrupted globular cluster that was orbiting around the progenitor of Cetus-Palca. The number of stars with spectroscopic measurements that fall on this feature and share a common orbital behaviour to Cetus-Palca is too small (7 stars) to establish with certainty its nature. The low scatter in metallicity (0.08 dex around a value  $[\text{Fe}/\text{H}] = -1.93$  dex) would support the globular cluster hypothesis. However, the distance gradient along this feature and the kinematics of its stars are very similar to those of the rest of

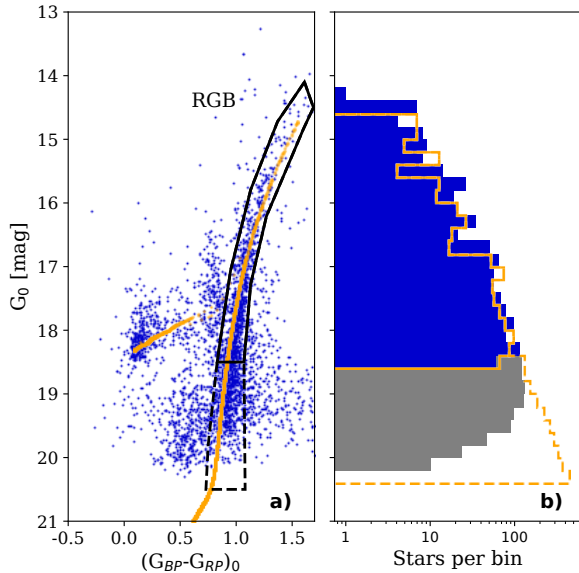


**Fig. 14.** *a)* CMD of the stars located in the Cetus-Palca selection box (blue rectangle in Fig. 12), overlaid with a 14 Gyr isochrone with a metallicity of  $[Fe/H]=-1.93$  (in orange). The black plain polygon shows the location of the RGB stars with the region where *Gaia* is complete, while the region where *Gaia* is not complete is shown by the dashed line polygon. *b)* Luminosity function of the RGB used to estimate the stellar mass of the Cetus-Palca stream (in blue), with the area affected by the drop of the completeness (in grey). The orange histogram shows the luminosity function of an  $1.5 \times 10^6 M_{\odot}$ ,  $[Fe/H]=-1.93$ , 14 old RGB population following a Kroupa mass function.

the Cetus-Palca spectroscopic sample. Only the line-of-sight velocity might be different than the other stars located along the main Cetus-Palca stream but with so few measurements, this is not a significant result. Therefore it is not possible to exclude the possibility that this second structure is actually another appendix of the Cetus-Palca stream itself. Such a structure could result, for instance, from the non-linear perturbations caused by the Large Magellanic Cloud (see Erkal et al. 2019; Shipp et al. 2019; Vasiliev et al. 2021, for discussions on the influence of the LMC on stellar streams).

To confirm (or disprove) the hypothesis of a second stream formed by the disruption of a globular cluster that was initially around the progenitor of Cetus-Palca, a spectroscopic follow-up is required to confirm that those stars do not present a scatter in metallicity, have a similar kinematic behaviour, and present the CNONaAl abundances anti-correlation, typical of old globular clusters (Carretta et al. 2010; Bastian & Lardo 2018). Should it be confirmed that this second structure is a second stream, this would be the first detected tidal stream of an object orbiting around a dwarf galaxy currently being itself disrupted, to the best of our knowledge. Such a discovery will be particularly crucial to constrain the initial profile of the dark matter halo of the Cetus-Palca dwarf galaxy (Malhan et al. 2021).

Two other stream-like structures are visible in Fig. 12, illustrated by the red ellipses in the upper panel. However, regarding the CMD of the Structure 1 in Fig. 13 we can see that it is a composition of the CMDs of the 2 control regions, which indicate that it is a structure of the disc, likely an artefact due to the high number of stars in that region close to the plan of the disc. For Structure 2, a red giant branch more distant than that of Cetus-Palca is visible, which actually corresponds to Sgr stream, whose track is shown by the light purple band in Fig. 12.

## 5. Summary and Conclusions

We presented a new method, based heavily on supervised machine learning, to derive accurate spectro-photometric distances with a high relative precision. Specifically, the method uses the *griz* photometric bands from the Pan-STARRS  $3\pi$  survey, the *G*-band from *Gaia* EDR3 and the effective temperature, surface gravity and metallicity derived from a given spectroscopic survey. This method will be used to derive distances for the stars observed by the Galactic Archaeology WEAVE surveys (Dalton et al. 2012) through the SPDIST *Contributed Data Product*. Meanwhile, we applied the technique on SDSS/SEGUE data and derive the distance of  $\sim 300,000$  stars in different evolutionary phases; the catalogue is available on the Vizier service of the Centre de Données Astronomique de Strasbourg (CDS). In its application to SDSS/SEGUE, the relative precision on the spectro-photometric distance is of 13%.

With the 6D sample obtained using these spectro-photometric distances, SEGUE line-of-sight velocities and *Gaia* EDR3 proper motions, we searched the integrals-of-motion plane and found a structure corresponding to the Cetus-Palca stellar stream (Newberg et al. 2009), hidden below the location of Sagittarius in the azimuthal and vertical actions (and energy and vertical angular momentum). This stellar structure however is clearly distinct from Sagittarius in its proper motion and radial velocity in the RA range  $10 - 35^{\circ}$ .

The good distance precision allowed us to integrate the orbits of these stars and to find the plane of the Cetus-Palca stream, which we then used to perform a detailed analysis, expanding the search for the Cetus-Palca stream to the whole sky, using the 5-D *Gaia* EDR3 sample. We measured a total extent of the stream of  $\approx 100^{\circ}$  on the sky over  $0$  to  $100^{\circ}$  in R.A. and over  $-80$  to  $65^{\circ}$  in DEC., overlapping with the Palca over-density detected by Shipp et al. (2018) in the Dark Energy Survey, as predicted by Chang et al. (2020). However, we did not find a northern counterpart, as suggested in the work of Yuan et al. (2019), possibly because of its diffuseness. The detected stream covers a heliocentric distance range between 25 and 40 kpc, it is metal-poor and presents a small scatter in metallicity ( $[Fe/H] = -1.93 \pm 0.21$ ) typical of a dwarf galaxy, consistent with previous measurements.

An analysis of the luminosity function leads to estimate the stellar mass of the Cetus-Palca progenitor to be of  $1.5 \times 10^6 M_{\odot}$ . This stellar mass is consistent with expectation from the stellar mass-metallicity relation of Local Group dwarf galaxies.

We also report the discovery of a second structure, almost parallel to the Cetus-Palca Stream, covering  $\sim 50^{\circ}$  of the sky and located at a similar heliocentric distance than Cetus-Palca. This could be a second stellar stream emanating from a globular cluster that was initially orbiting around the Cetus-Palca progenitor, now completely disrupted. However, at this stage, without further spectroscopic information, it is not possible to exclude the hypothesis that this second structure is reflecting the complex structure of the Cetus-Palca stream, and that it is actually a part of the Cetus-Palca stream itself.

*Acknowledgements.* The authors thank Rodrigo Ibata and Eduardo Balbinot for useful discussions, as well as the anonymous referee for comments that increased the clarity of the publication. GT acknowledges support from the Agencia Estatal de Investigación (AEI) of the Ministerio de Ciencia e Innovación (MCINN) under grant FJC2018-037323-I. The authors acknowledge financial support through the grant (AEI/FEDER, UE) AYA2017-89076-P, as well as by the Ministerio de Ciencia, Innovación y Universidades (MCIU), through the State Budget and by the Consejería de Economía, Industria, Comercio y Conocimiento of the Canary Islands Autonomous Community, through the Regional Budget.

## References

- Anders, F., Khalatyan, A., Chiappini, C., et al. 2019, arXiv e-prints, 1904, arXiv:1904.11302
- Bailer-Jones, C. A. L. 2015, Publications of the Astronomical Society of the Pacific, 127, 994
- Bailer-Jones, C. A. L., Rybizki, J., Founesneau, M., Mantelet, G., & Andrae, R. 2018, The Astronomical Journal, 156, 58
- Bastian, N. & Lardo, C. 2018, Annual Review of Astronomy and Astrophysics, vol. 56, p.83-136, 56, 83
- Battaglia, G., Taibi, S., Thomas, G. F., & Fritz, T. K. 2021, Gaia Early DR3 Systemic Motions of Local Group Dwarf Galaxies and Orbital Properties with a Massive Large Magellanic Cloud
- Belokurov, V., Erkal, D., Evans, N. W., Koposov, S. E., & Deason, A. J. 2018, Monthly Notices of the Royal Astronomical Society, 478, 611
- Belokurov, V., Koposov, S. E., Evans, N. W., et al. 2014, Monthly Notices of the Royal Astronomical Society, 437, 116
- Boubert, D. & Everall, A. 2020, Monthly Notices of the Royal Astronomical Society, 497, 4246
- Cargile, P. A., Conroy, C., Johnson, B. D., et al. 2020, The Astrophysical Journal, 900, 28
- Carretta, E., Bragaglia, A., Gratton, R. G., et al. 2010, Astronomy and Astrophysics, Volume 516, id.A55, <NUMPAGES>29</NUMPAGES> pp., 516, A55
- Chambers, K. C., Magnier, E. A., Metcalfe, N., et al. 2016, ArXiv e-prints, 1612, arXiv:1612.05560
- Chang, J., Yuan, Z., Xue, X.-X., et al. 2020, The Astrophysical Journal, 905, 100
- Choi, J., Dotter, A., Conroy, C., et al. 2016, The Astrophysical Journal, 823, 102
- Chollet, F. 2015, Keras
- Clementini, G., Ripepi, V., Molinaro, R., et al. 2019, Astronomy & Astrophysics, Volume 622, id.A60, <NUMPAGES>37</NUMPAGES> pp., 622, A60
- Collaboration, G., Eyer, L., Rimoldini, L., et al. 2019, Astronomy and Astrophysics, 623, A110
- Conroy, C., Bonaca, A., Cargile, P., et al. 2019a, The Astrophysical Journal, 883, 107
- Conroy, C., Naidu, R. P., Garavito-Camargo, N., et al. 2021, Nature, 592, 534
- Conroy, C., Naidu, R. P., Zaritsky, D., et al. 2019b, The Astrophysical Journal, 887, 237
- Coronado, J., Rix, H.-W., & Trick, W. H. 2018, Monthly Notices of the Royal Astronomical Society, 481, 2970
- Dalton, G., Trager, S. C., Abrams, D. C., et al. 2012, 8446, 84460P
- de Boer, T. J. L., Tolstoy, E., Hill, V., et al. 2012, Astronomy & Astrophysics, Volume 539, id.A103, <NUMPAGES>18</NUMPAGES> pp., 539, A103
- de Vaucouleurs, G. 1958, The Astrophysical Journal, 128, 465
- Deason, A. J., Belokurov, V., & Evans, N. W. 2011, Monthly Notices of the Royal Astronomical Society, 416, 2903
- Dehnen, W. & Binney, J. 1998, Monthly Notices of the Royal Astronomical Society, 294, 429
- Dotter, A. 2016, The Astrophysical Journal Supplement Series, 222, 8
- Eilers, A.-C., Hogg, D. W., Rix, H.-W., & Ness, M. K. 2019, The Astrophysical Journal, 871, 120
- Erkal, D., Belokurov, V., Laporte, C. F. P., et al. 2019, Monthly Notices of the Royal Astronomical Society, 487, 2685
- Fernández-Alvar, E., Allende Prieto, C., Beers, T. C., et al. 2016, Astronomy & Astrophysics, Volume 593, id.A28, <NUMPAGES>9</NUMPAGES> pp., 593, A28
- Fernández-Alvar, E., Kordopatis, G., Hill, V., et al. 2021, The Pristine Survey XIV: Uncovering the Very Metal-Poor Tail of the Thin Disc
- Flaugher, B. & Bebek, C. 2014, 9147, 91470S
- Foreman-Mackey, D., Hogg, D. W., Lang, D., & Goodman, J. 2013, Publications of the Astronomical Society of the Pacific, 125, 306
- Fukushima, T., Chiba, M., Homma, D., et al. 2018, Publications of the Astronomical Society of Japan, 70, 69
- Fukushima, T., Chiba, M., Tanaka, M., et al. 2019, arXiv e-prints, 1904, arXiv:1904.04966
- Gaia Collaboration. 2016, Astronomy and Astrophysics, 595, A1
- Gaia Collaboration, Brown, A. G. A., Vallenari, A., et al. 2020, arXiv e-prints, 2012, arXiv:2012.01533
- Gaia Collaboration, G. 2018, Astronomy and Astrophysics, 616, A1
- Gravity Collaboration, Abuter, R., Amorim, A., et al. 2018, Astronomy and Astrophysics, 615, L15
- Harris, W. E. 2010, arXiv e-prints, 1012, arXiv:1012.3224
- Haywood, M., Di Matteo, P., Lehnert, M. D., et al. 2018, The Astrophysical Journal, 863, 113
- Helmi, A. & White, S. D. M. 1999, Monthly Notices of the Royal Astronomical Society, 307, 495
- Hernitschek, N., Cohen, J. G., Rix, H.-W., et al. 2018, The Astrophysical Journal, 859, 31
- Hogg, D. W., Eilers, A.-C., & Rix, H.-W. 2018, arXiv e-prints, arXiv:1810.09468
- Holl, B., Audard, M., Nienartowicz, K., et al. 2018, Astronomy & Astrophysics, Volume 618, id.A30, <NUMPAGES>21</NUMPAGES> pp., 618, A30
- Ibata, R., Bellazzini, M., Thomas, G., et al. 2020, The Astrophysical Journal Letters, 891, L19
- Ibata, R., Irwin, M., Lewis, G., Ferguson, A. M. N., & Tanvir, N. 2001, Nature, 412, 49
- Ibata, R., Malhan, K., Martin, N., et al. 2021, The Astrophysical Journal, 914, 123
- Ibata, R. A., Gilmore, G., & Irwin, M. J. 1994, Nature, 370, 194
- Ibata, R. A., McConnachie, A., Cuillandre, J.-C., et al. 2017, The Astrophysical Journal, 848, 129
- Iorio, G. & Belokurov, V. 2019, Monthly Notices of the Royal Astronomical Society, 482, 3868
- Irwin, M. & Hatzidimitriou, D. 1995, Monthly Notices of the Royal Astronomical Society, 277, 1354
- Ishigaki, M. N., Hartwig, T., Tarumi, Y., et al. 2021, Monthly Notices of the Royal Astronomical Society, 506, 5410
- Ivezić, Ž., Sesar, B., Jurić, M., et al. 2008, The Astrophysical Journal, 684, 287
- Jean-Baptiste, I., Di Matteo, P., Haywood, M., et al. 2016, ArXiv e-prints, 1611, arXiv:1611.07193
- Jurić, M., Ivezić, Ž., Brooks, A., et al. 2008, The Astrophysical Journal, 673, 864
- Kingma, D. P. & Ba, J. 2014, arXiv e-prints, 1412, arXiv:1412.6980
- Kirby, E. N., Cohen, J. G., Guhathakurta, P., et al. 2013, The Astrophysical Journal, 779, 102
- Kollmeier, J. A., Zasowski, G., Rix, H.-W., et al. 2017, SDSS-V: Pioneering Panoptic Spectroscopy
- Koposov, S. E., Belokurov, V., Evans, N. W., et al. 2012, The Astrophysical Journal, 750, 80
- Koposov, S. E., Belokurov, V., Li, T. S., et al. 2019, Monthly Notices of the Royal Astronomical Society, 485, 4726
- Koposov, S. E., Rix, H.-W., & Hogg, D. W. 2010, The Astrophysical Journal, 712, 260
- Kroupa, P. 2001, Monthly Notices of the Royal Astronomical Society, 322, 231
- Kruijssen, J. M. D., Pfeffer, J. L., Chevance, M., et al. 2020, Monthly Notices of the Royal Astronomical Society, 498, 2472
- Lane, J. M. M., Bovy, J., & Mackereth, J. T. 2021, The Kinematic Properties of Milky Way Stellar Halo Populations
- Lee, Y. S., Beers, T. C., Sivarani, T., et al. 2008, The Astronomical Journal, 136, 2022
- Liao, S.-L., Qi, Z.-X., Guo, S.-F., & Cao, Z.-H. 2019, Research in Astronomy and Astrophysics, 19, 029
- Lindgren, L., Klioner, S. A., Hernández, J., et al. 2020, arXiv e-prints, 2012, arXiv:2012.03380
- Łokas, E. L. 2009, Monthly Notices of the Royal Astronomical Society, 394, L102
- Longeard, N., Martin, N., Starkenburg, E., et al. 2018, Monthly Notices of the Royal Astronomical Society, 480, 2609
- Luri, X., Brown, A. G. A., Sarro, L. M., et al. 2018, Astronomy and Astrophysics, 616, A9
- Magnier, E. A., Chambers, K. C., Flewelling, H. A., et al. 2020a, The Astrophysical Journal Supplement Series, 251, 3
- Magnier, E. A., Sweeney, W. E., Chambers, K. C., et al. 2020b, 251, 5
- Majewski, S. R., Skrutskie, M. F., Weinberg, M. D., & Ostheimer, J. C. 2003, The Astrophysical Journal, 599, 1082
- Malhan, K. & Ibata, R. A. 2018, Monthly Notices of the Royal Astronomical Society, 477, 4063
- Malhan, K., Yuan, Z., Ibata, R. A., et al. 2021, The Astrophysical Journal, 920, 51
- Marigo, P., Girardi, L., Bressan, A., et al. 2008, Astronomy and Astrophysics, 482, 883
- Martin, N. F., Ibata, R. A., McConnachie, A. W., et al. 2013, The Astrophysical Journal, 776, 80
- McConnachie, A. W. 2012, The Astronomical Journal, 144, 4
- McConnachie, A. W. & Venn, K. A. 2020a, The Astronomical Journal, 160, 124
- McConnachie, A. W. & Venn, K. A. 2020b, Research Notes of the American Astronomical Society, 4, 229
- McMillan, P. J. 2017, Monthly Notices of the Royal Astronomical Society, 465, 76
- McMillan, P. J., Kordopatis, G., Kunder, A., et al. 2018, Monthly Notices of the Royal Astronomical Society, 477, 5279
- Muraveva, T., Delgado, H. E., Clementini, G., Sarro, L. M., & Garofalo, A. 2018, Monthly Notices of the Royal Astronomical Society, 481, 1195
- Myeong, G. C., Evans, N. W., Belokurov, V., Amorisco, N. C., & Koposov, S. E. 2018a, Monthly Notices of the Royal Astronomical Society, 475, 1537
- Myeong, G. C., Evans, N. W., Belokurov, V., Sanders, J. L., & Koposov, S. E. 2018b, The Astrophysical Journal, 856, L26



- Myeong, G. C., Evans, N. W., Belokurov, V., Sanders, J. L., & Koposov, S. E. 2018c, *The Astrophysical Journal Letters*, 863, L28
- Myeong, G. C., Vasiliev, E., Iorio, G., Evans, N. W., & Belokurov, V. 2019, *Monthly Notices of the Royal Astronomical Society*, 488, 1235
- Naidu, R. P., Conroy, C., Bonaca, A., et al. 2020, *The Astrophysical Journal*, 901, 48
- Newberg, H. J., Yanny, B., & Willett, B. A. 2009, *The Astrophysical Journal Letters*, 700, L61
- Pace, A. B. & Li, T. S. 2019, *The Astrophysical Journal*, 875, 77
- Pieres, A., Girardi, L., Balbinot, E., et al. 2019, arXiv e-prints, arXiv:1904.04350
- Price-Whelan, A. M. 2017, *The Journal of Open Source Software*, 2, 388
- Queiroz, A. B. A., Anders, F., Santiago, B. X., et al. 2018, *Monthly Notices of the Royal Astronomical Society*, 476, 2556
- Schlafly, E. F. & Finkbeiner, D. P. 2011, *The Astrophysical Journal*, 737, 103
- Schlegel, D. J., Finkbeiner, D. P., & Davis, M. 1998, *The Astrophysical Journal*, 500, 525
- Schönrich, R., Binney, J., & Dehnen, W. 2010, *Monthly Notices of the Royal Astronomical Society*, 403, 1829
- Sesar, B., Hermitschek, N., Mitrović, S., et al. 2017, *The Astronomical Journal*, 153, 204
- Sestito, F., Longeard, N., Martin, N. F., et al. 2019, *Monthly Notices of the Royal Astronomical Society*, 46
- Shipp, N., Drlica-Wagner, A., Balbinot, E., et al. 2018, *The Astrophysical Journal*, 862, 114
- Shipp, N., Li, T. S., Pace, A. B., et al. 2019, *The Astrophysical Journal*, 885, 3
- Simpson, J. D., Martell, S. L., Buder, S., et al. 2021, *Monthly Notices of the Royal Astronomical Society*, 507, 43
- Sirko, E., Goodman, J., Knapp, G. R., et al. 2004, *The Astronomical Journal*, 127, 899
- Starkenburg, E., Martin, N., Youakim, K., et al. 2017, *Monthly Notices of the Royal Astronomical Society*, 471, 2587
- Starkenburg, E., Youakim, K., Martin, N., et al. 2019, *Monthly Notices of the Royal Astronomical Society*, 490, 5757
- Thomas, G. F., Annau, N., McConnachie, A., et al. 2019a, *The Astrophysical Journal*, 886, 10
- Thomas, G. F., Laporte, C. F. P., McConnachie, A. W., et al. 2019b, *Monthly Notices of the Royal Astronomical Society*, 483, 3119
- Thomas, G. F., McConnachie, A. W., Ibata, R. A., et al. 2018, *Monthly Notices of the Royal Astronomical Society*
- Tremblay, P.-E., Ludwig, H.-G., Steffen, M., & Freytag, B. 2013, *Astronomy and Astrophysics*, 559, A104
- Vasiliev, E. 2018, arXiv e-prints, 1802, arXiv:1802.08255
- Vasiliev, E., Belokurov, V., & Erkal, D. 2021, *Monthly Notices of the Royal Astronomical Society*, 501, 2279
- Vickers, J. J., Grebel, E. K., & Huxor, A. P. 2012, *The Astronomical Journal*, 143, 86
- Xue, X.-X., Ma, Z., Rix, H.-W., et al. 2014, *The Astrophysical Journal*, 784, 170
- Xue, X.-X., Rix, H.-W., Yanny, B., et al. 2011, *The Astrophysical Journal*, 738, 79
- Xue, X. X., Rix, H. W., Zhao, G., et al. 2008, *The Astrophysical Journal*, 684, 1143
- Yam, W., Carlin, J. L., Newberg, H. J., et al. 2013, *The Astrophysical Journal*, 776, 133
- Yanny, B., Newberg, H. J., Johnson, J. A., et al. 2009, *The Astrophysical Journal*, 700, 1282
- Yuan, Z., Smith, M. C., Xue, X.-X., et al. 2019, *The Astrophysical Journal*, 881, 164
- Zhao, G., Zhao, Y., Chu, Y., Jing, Y., & Deng, L. 2012, *LAMOST Spectral Survey*

## Appendix A: Spectro-photometric distances with different training set

We present here the improvement on the distance measurement made by the addition of the K-giant catalogue of [Xue et al. \(2014\)](#) and of the BHB catalogue from [Xue et al. \(2008\)](#) to the training sample of the ANN used to derived spectro-photometric distances, which motivated our choices in the construction of the final training sample used by the ANN presented in Section 2.

On Fig. A.1, we present the expected and predicted colour magnitude diagrams for the different training samples made with the addition of K-giants and BHBs to stars selected from their parallax.

The general accuracy of the ANN is the same for the different training samples because they are composed mainly of main sequence stars (>80%, but the actual number differ slightly between the training samples), and these are the same between the different training samples. However, the global shape of the CMDs is different, especially for the top part of the red giant branch ( $M_G \lesssim -1$ ). Indeed, without the inclusion of the K-giants to the training sample, the predicted absolute magnitudes tend to a plateau around  $M_G = -1$ , and the red giant branch is globally less well-defined. This is because in the training sample based only on the parallaxes, the stars on the red giant branch have a low relative precision on their parallax. Nevertheless, it is interesting to see that for all cases, the ANN improves the shape of the predicted CMD compared to the expected one, with a clear separation between giants and sub-giants for example (around  $0.8 \leq (\text{BP-RP})_0 \leq 1.2$  and  $2 \leq M_G \leq 4$ ).

The inclusion of the BHBs to the training sample have a small effect on the better definition of the horizontal branch. However, its effect is far from marginal, since without its inclusion, the absolute magnitude predicted for the BHB stars is on average  $\approx 0.2$  magnitude fainter than measured with the distance calibration of [Deason et al. \(2011\)](#), leading to a systematic overestimation of the distance (or accuracy error) of  $\approx 10\%$ .

## Appendix B: Precision of the spectro-photometric distances as function of $T_{eff}$ , $\log(g)$ and $[\text{Fe}/\text{H}]$

The mean relative precision on the distance predicted by the ANN presented in Section 2.2 is 13%, or 0.27 mag, but the actual precision varies for stars with different effective temperature, surface gravity and metallicity. To analyse the precision of the spectro-photometric distances over these three parameters, we selected stars of the training sample located in different regions of the parameter space, and we fitted a Gaussian function to their  $\Delta M_G = M_{true} - M_{predicted}$  histogram. The variation of the precision of the residual absolute magnitude with the effective temperature, surface gravity and metallicity is presented in Figure B.1.

**Precision as function of the effective temperature** The variation of the residual between the “true” and predicted absolute magnitude as a function of the effective temperature is presented in the upper panel of Figure B.1, where the bins in effective temperature have a width of 500 K. One can see that between  $4000 < T_{eff} < 7500$  K, the residual is relatively flat with a typical scatter of 0.26 mag, slightly rising to a scatter of 0.36 mag at  $T_{eff} = 7250$  K, due to the low number of stars in that range, making harder to have a good fit to the distance in that range. Beyond 7500 K, the precision increases drastically, with the scatter between the “true” and the predicted absolute magnitude going

down to 0.05 mag. This is because in that range, more than 2/3 of the stars of the training sample are BHBs that have a low intrinsic scatter ( $< 0.1$  mag [Deason et al. 2011](#)), making it easier to have a precise predicted absolute magnitude for these stars.

**Precision as function of the surface gravity** The middle panel of Figure B.1 shows the evolution of the residual absolute magnitude with the surface gravity, where the bins in surface gravity have a width of  $\log(g) = 0.5$  dex. The residual is relatively constant over the range of surface gravity predicted by SEGUE, except toward  $\log(g) = 0.5$  dex where the predicted magnitudes are overestimated by 0.18 mag and the scatter of the residual goes to 0.42 mag. This is due to the very low number of stars in that range and to the poor determination of the surface gravity by the SSPP in that range, as illustrate the numerous clumps of stars with exactly the surface gravity values in that surface gravity range. It has to be noticed here that the trend for the K-giants, shown by the blue dots, is similar to the trend of the global training set for  $\log(g) > 2.5$  dex since they constitute the majority of the training sample in that range. Between  $2.5 < \log(g) < 3.0$  dex, the difference between the “true” and the predicted absolute magnitude is also abnormally high, with a scatter of 0.58 mag. In that range of surface gravity, the large majority of the stars of the training sample (87%) have been selected based on their absolute parallax precision ( $\delta\varpi < 0.07$  mas), and are not part of the K-giant catalogue of [Xue et al. \(2014\)](#), nor of the BHB catalogue of [Xue et al. \(2008\)](#). For this reason, the “true” absolute magnitudes of the stars of the training sample are not well-defined in that surface gravity range, with an average uncertainties on the “true” absolute magnitude of  $\delta M_G = 0.94$  mag, rather than  $\delta M_G = 0.26$  mag for the global training sample. This low precision of the “true” absolute magnitudes explains by itself the increase of the scatter of the residual. However, the precision on the predicted absolute magnitude in that range of surface gravity is likely similar than for the rest of the stars since we found a scatter of the residual of 0.30 mag for the 229 (over 3, 715) stars with  $\varpi/\delta\varpi \geq 10$  located in that region, but with predicted absolute magnitudes systematically underestimated of 0.1 mag, as shows the green triangle in Figure B.1. In comparison, for the 355 K-giants located in that region, the predicted absolute magnitudes are systematically over-estimated of 0.2 mag, with a scatter on the residual of 0.37 mag. However, this comparison has to be taken with a pinch of salt since the K-giants in that region have a typical uncertainty on their “true” absolute magnitude of  $\delta M_G = 0.42$  mag, higher than for the rest of the K-giants ( $M_G = 0.32$  mag). Regarding the results of this analysis, we cannot definitively conclude that the precision on the absolute magnitude (distance) between  $2.5 < \log(g) < 3.0$  dex is similar than for other surface gravity ranges, and the distances estimated for the stars in that range have to be taken with a pinch of salt.

**Precision as function of the metallicity** The variation residual absolute magnitude between the “true” and the predicted one as a function of the metallicity is presented in the lower panel of Figure B.1, where the bins in metallicity have a width of  $[\text{Fe}/\text{H}] = 0.1$ . The scatter is constant (typically of 0.28 mag) over almost the full range of metallicities, with a small increase toward the low metallicity edges, caused by the low number of stars in that region and the imprecision of the metallicities predicted by the SSPP for extremely metal-poor stars (see [Fernández-Alvar et al. 2016](#); [Starkenburger et al. 2017](#)). Around  $[\text{Fe}/\text{H}] \approx -0.1$ , the scatter of the residual is of 0.17 mag, lower than for other metallicities because in that region the stars of the

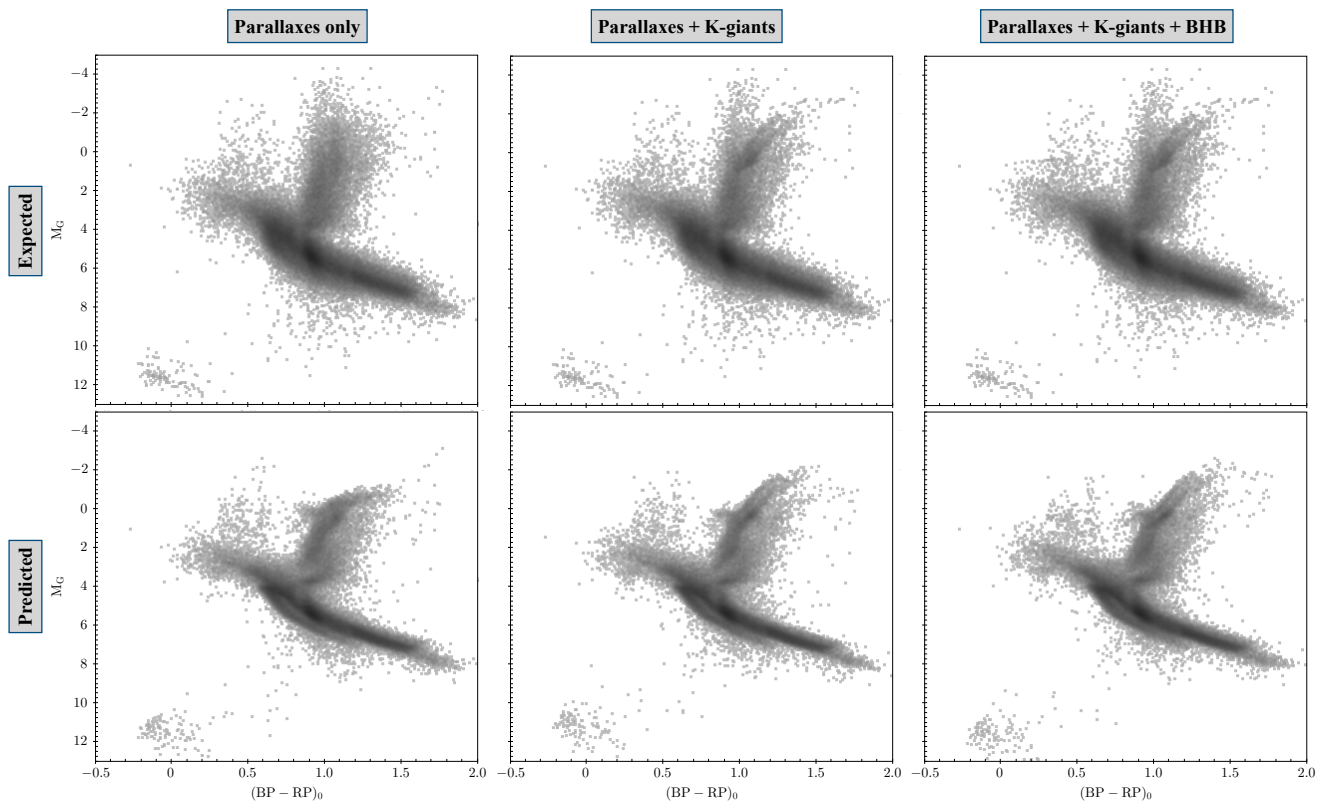


**Fig. A.1.** The upper panels show the expected  $(BP-RP)_0 - M_G$  colour magnitude diagrams for a training sample composed only of stars that respect the parallax criteria presented in Section 2.2 (on the left), with the inclusion of K-giants (in the middle), and with the inclusion of both K-giants and BHBs (on the right). We only show the stars in common between the different samples, since the number of stars used to train the ANN are different from one to another training sample due to the different constraints used to create them. The lower panels show the corresponding colour magnitude diagrams with the absolute magnitude  $M_G$  predicted by the ANN. We can clearly see the improvement made by the inclusion of the different catalogues on the global shape of the CMD, especially from the K-giants.

training sample have a typical uncertainty on the “true” absolute magnitude  $\delta M_G = 0.15$  mag lower than for the rest of the stars of the training sample  $\delta M_G = 0.26$  mag.



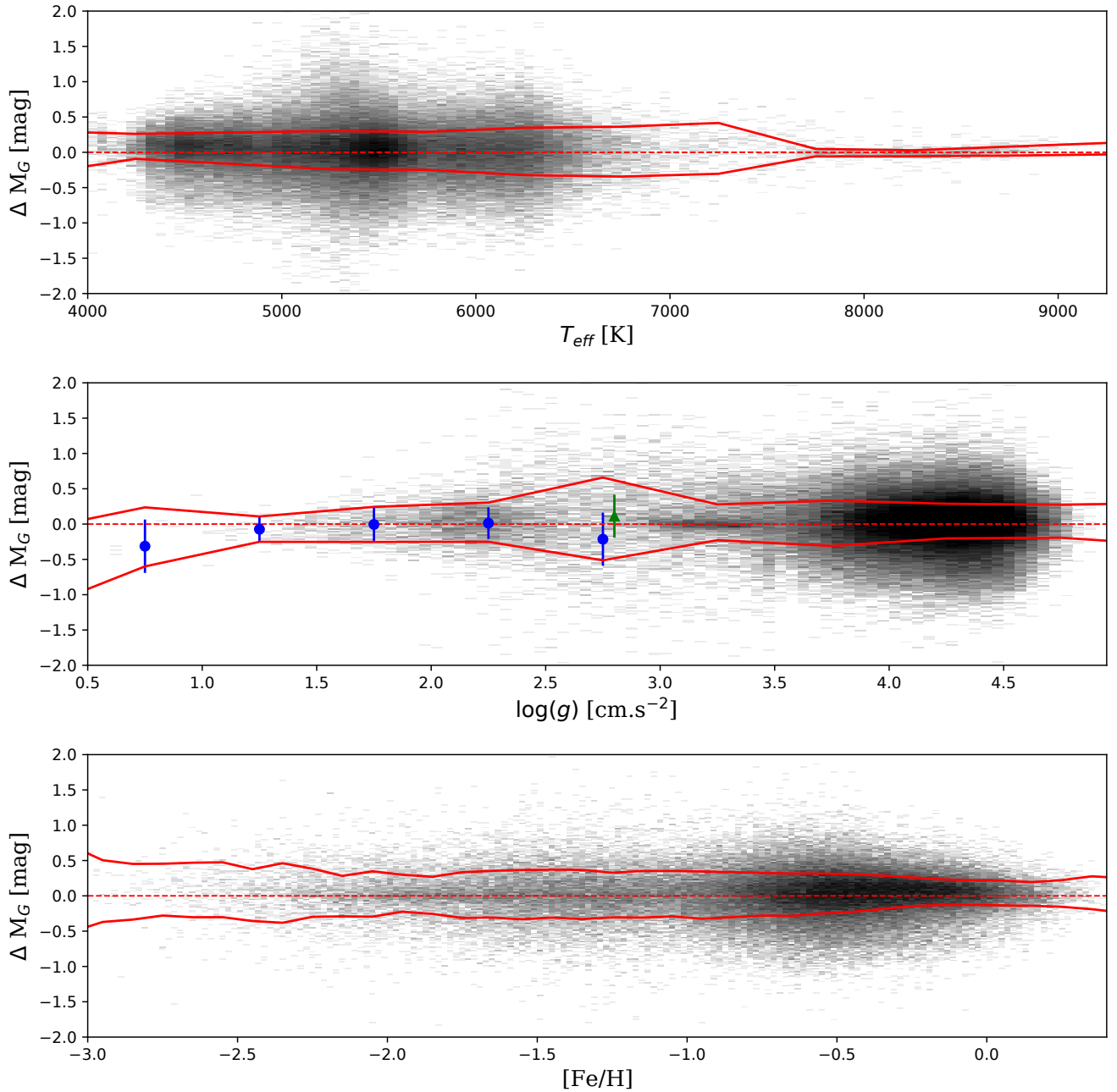


**Fig. B.1.** Variation of the residual between the “true” and predicted absolute magnitudes with the effective temperature (upper panel), the surface gravity (middle panel) and the metallicity (lower panel). The dotted line shows cases the predicted and the “true” absolute magnitude are equal. The red continuous line shows the variation of this residual as a function of these parameters. In the middle panel, the blue dots show the evolution of the residual for the K-giant stars of the catalogue of [Xue et al. \(2014\)](#), and the green triangle shows it for the 229 stars between  $2.5 < \log(g) < 3.0$  dex and with relative precision on their parallax of  $\varpi/\delta\varpi \geq 10$ .